Lack of CCDC146, a ubiquitous centriole and microtubule-associated protein, leads to non-syndromic male infertility in human and mouse

Jana Muroňová[1,2,3,†], Zine-Eddine Kherraf[1,2,3,4,†], Elsa Giordani[1,2,3], Simon Eckert[5], Caroline Cazin[1,2,3,4], Amir Amiri-Yekta[1,2,3,4], Emeline lambert[1,2,3], Geneviève Chevalier[1,2,3], Guillaume Martinez[1,2,3,6], Yasmine Neirijnck[7], Francoise Kühne[7], Lydia Wehrli[7], Nikolai Klena[8,9], Virginie Hamel[8], Jessica Escoffier[1,2,3], Paul Guichard[8], Charles Coutton[1,2,3,6], Selima Fourati Ben Mustapha[10], Mahmoud Kharouf[10], Raoudha Zouari[10], Nicolas Thierry-Mieg[11], Serge Nef[7], Stefan Geimer[5], Corinne Loeuillet[1,2,3], Pierre Ray[1,2,3,4,‡], Christophe Arnoult[1,2,3,‡,*]

[1]Institute for Advanced Biosciences, (IAB), INSERM 1209,

[2] Institute for Advanced Biosciences, (IAB) CNRS UMR 5309

[3] Institute for Advanced Biosciences, (IAB) Université Grenoble Alpes

[4]UM GI-DPI, CHU Grenoble Alpes, F-38000 Grenoble, France

[5] Cell Biology/ Electron Microscopy, University of Bayreuth, 95440 Bayreuth, Germany

[6]UM de Génétique Chromosomique, Hôpital Couple-Enfant, CHU Grenoble Alpes, F-38000 Grenoble, France

[7]Department of Genetic Medicine and Development, University of Geneva Medical School, Geneva 1211, Switzerland

[8] University of Geneva, Department of Molecular and Cellular Biology, Sciences III, Geneva, Switzerland

[9]Present address: Human Technopole, 20157 Milan, Italy

[10]Polyclinique les Jasmins, Centre d'Aide Médicale à la Procréation, Centre Urbain Nord, 1003 Tunis, Tunisia

[11] Laboratoire TIMC/MAGe, CNRS UMR 5525, Pavillon Taillefer, Faculté de Medecine, 38700 La Tronche, France

†These authors contributed equally to this work

‡These authors contributed equally to this work as senior authors

*Correspondence: christophe.arnoult@univ-grenoble-alpes.fr or PRay@chu-grenoble.fr

Abstract

Genetic mutations are a recurrent cause of male infertility. Multiple morphological abnormalities of the flagellum (MMAF) syndrome is a heterogeneous genetic disease, with which more than 50 genes have been linked. Nevertheless, for 50% of patients with this condition, no genetic cause is identified. From a study of a cohort of 167 MMAF patients, pathogenic bi-allelic mutations were identified in the *CCDC146* gene in two patients. This gene encodes a poorly characterized centrosomal protein which we studied in detail here. First, protein localization was studied in two cell lines. We confirmed the centrosomal localization in somatic cells and showed that the protein also presents multiple microtubule-related localizations during mitotic division, suggesting that it is a microtubule-associated protein (MAP). To better understand the function of the protein at the sperm level, and the molecular pathogenesis of infertility associated with *CCDC146* mutations, two genetically modified mouse models were created: a *Ccdc146* knock-out (KO) and a knock-in (KI) expressing a HA-tagged CCDC146 protein. KO male mice were completely infertile, and sperm exhibited a phenotype identical to our two MMAF patient's phenotype with *CCDC146* mutations. No other pathology was observed, and the animals were viable. CCDC146 expression starts during late spermiogenesis, at the time of flagellum biogenesis. In the spermatozoon, the protein is conserved but is not localized to centrioles, unlike in somatic cells, rather it is present in the axoneme at the level of microtubule doublets. Expansion microscopy associated with the use of the detergent sarkosyl to solubilize microtubule doublets, provided evidence that the protein could be a microtubule inner protein (MIP). At the subcellular level, the absence of CCDC146 affected the formation, localization and morphology of all microtubule-based organelles such as the manchette, the head–tail coupling apparatus (HTCA), and the axoneme. Through this study, we have characterized a new genetic cause of infertility, identified a new factor in the formation and/or structure of the sperm axoneme, and demonstrated that the CCDC146 protein plays several cellular roles, depending on the cell type and the stages in the cell cycle.

Introduction

Infertility is a major health concern, affecting approximately 50 million couples worldwide [1], or 12.5% of women and 10% of men. It is defined by the World Health Organization (WHO) as the "failure to achieve a pregnancy after 12 months or more of regular unprotected sexual intercourse". In almost all countries, infertile couples have access to assisted reproductive technology (ART) to try to conceive

64 a baby, and there are now 5 million people born as a result of ART. Despite this success, almost half of
65 the couples seeking medical support for infertility fails to successfully conceive and bear a child by the
66 end of their medical care. The main reason for these failures is that one member of the couple
67 produces gametes that are unable to support fertilization and/or embryonic development. Indeed,
68 ART does not specifically treat or even try to elucidate the underlying causes of a couple's infertility,
69 rather it tries to bypass the observed defects. Consequently, when defects in the gametes cannot be
70 circumvented by the techniques currently proposed, ART fails. To really treat infertility, a first step
71 would be to gain a better understanding of the problems with gametogenesis for each patient. This
72 type of approach should increase the likelihood of adopting the best strategy for affected patients, and
73 if necessary, should guide the development of innovative therapies.

74 Male infertility has several causes, such as infectious diseases, anatomical defects, or a genetic
75 deficiency. Genetic defects play a major role in male infertility, with over 4000 genes thought to be
76 involved in sperm production, of which more than 2000 are testis-enriched and almost exclusively
77 involved in spermatogenesis [2]. Mutations in any of these genes can negatively affect
78 spermatogenesis and produce one of many described sperm disorders. The characterization and
79 identification of the molecular bases of male infertility is thus a real challenge. Nevertheless, thanks to
80 the emergence of massively parallel sequencing technologies, such as whole exome sequencing (WES)
81 and whole genome sequencing (WGS), the identification of genetic defects has been greatly facilitated
82 in recent years. As a consequence, remarkable progress has been made in the characterization of
83 numerous human genetic diseases, including male infertility.

84 Today, more than 120 genes are associated with all types of male infertility [3], including
85 quantitative and qualitative sperm defects. Qualitative spermatogenesis defects impacting sperm
86 morphology, also known as "teratozoospermia"[4, 5], are a heterogeneous group of abnormalities
87 covering a wide range of sperm phenotypes. Among these phenotypes, some relate to the morphology
88 of the flagellum. These defects are usually not uniform, and patients' sperm show a wide range of
89 flagellar morphologies such as short and/or coiled and/or irregularly sized flagella. Due to this
90 heterogeneity, this phenotype is now referred to as multiple morphological abnormalities of the sperm
91 flagellum (MMAF)[5]. Sperm from these patients are generally immotile, and patients are sterile.

92 Given the number of proteins present in the flagellum and necessary for its formation and
93 functioning, many genes have already been linked to the MMAF phenotype. Study of the MMAF
94 phenotype in humans has allowed the identification of around 50 genes [6] coding for proteins
95 involved in axonemal organization, present in the structures surrounding the axoneme – such as the
96 outer dense fibers and the fibrous sheath – and involved in intra-flagellar transport (IFT). Moreover,

97 some genes have been identified from mouse models, and their human orthologs are very good gene
98 candidates for MMAF, even if no patient has yet been identified with mutations in these genes. Finally,
99 based on the remarkable structural similarity of the axonemal structure of motile cilia and flagella,
100 some MMAF genes were initially identified in the context of primary ciliary dyskinesia (PCD). However,
101 this structural similarity does not necessarily imply a molecular similarity, and only around half (10 of
102 the 22 PCD-related genes identified so far [7]) are effectively associated with male infertility. However,
103 in most cases, the number of patients is very low and the details of the sperm tail phenotype are
104 unknown [7].

105 We have recruited 167 patients with MMAF. Following whole exome sequencing, biallelic
106 deleterious variants in 22 genes were identified in 83 subjects. The genes identified are *AK7*[8], *ARMC2*
107 [9], *CFAP206* [10], *CCDC34* [11], *CFAP251* [12], *CFAP43* and *CFAP44* [13], *CFAP47* [14], *CFAP61* [15],
108 *CFAP65* [16], *CFAP69* [17], *CFAP70* [18], *CFAP91* [19], *CFAP206* [10], *DNAH1* [20], *DNAH8* [21], *FSIP2*
109 [22], *IFT74* [23], *QRICH2* [24], *SPEF2* [25], *TTC21A* [26] and *TTC29* [27]. Despite this success, a molecular
110 diagnosis is obtained in half of the patients (49.7%) with this sperm phenotype, suggesting that novel
111 candidate genes remain to be identified. We have pursued our effort with this cohort to identify
112 further mutations that could explain the patient MMAF phenotype. As such, we have identified bi-
113 allelic truncating mutations in *CCDC146* in two unrelated infertile patients displaying MMAF. *CCDC146*
114 *is* known to code for a centrosomal protein when heterologously expressed in HeLa cells [28, 29], but
115 minimal information is available on its distribution within the cell, or its function when naturally
116 present. Moreover, this gene has never been associated with any human disease.

117 The centrosome, located adjacent to the nucleus, is a microtubule-based structure composed of a
118 pair of orthogonally-oriented centrioles surrounded by the pericentriolar material (PCM). The
119 centrosome is the major microtubule-organizing center (MTOC) in animal cells, and as such regulates
120 the microtubule organization within the cell. Therefore, it controls intracellular organization and
121 intracellular transport, and consequently regulates cell shape, cell polarity, and cell migration. The
122 centrosome is also crucial for cell division as it controls the assembly of the mitotic/meiotic spindle,
123 ensuring correct segregation of sister chromatids in each of the daughter cells [30]. The importance of
124 this organelle is highlighted by the fact that 3% (579 proteins) of all known human proteins have been
125 experimentally detected in the centrosome
126 (https://www.proteinatlas.org/humanproteome/subcellular/centrosome). Centrioles also play
127 essential roles in spermatogenesis and particularly during spermiogenesis. In round spermatids, the
128 centriole pair docks to the cell membrane, whereas the distal centriole serves as the basal body
129 initiating assembly of the axoneme. The proximal centriole then tightly attaches to the sperm nucleus
130 and gradually develops the head-to-tail coupling apparatus (HTCA), linking the sperm head to the

flagellum [31]. In human and bovine sperm, the proximal centriole is retained and the distal centriole is remodeled to produce an 'atypical' centriole [32]; in contrast, in rodents, both centrioles are degenerated during epididymal maturation [33]. Despite the number of proteins making up the centrosome, and its importance in sperm differentiation and flagellum formation, very few centrosomal proteins have been linked to MMAF in humans – so far only CEP135 [34], CEP148 [35] or DZIP1 [36]. Moreover, some major axonemal proteins with an accessory location in the centrosome, such as CFAP58 [37] and ODF2 [38, 39], have also been reported to be involved in MMAF syndrome. Other centrosomal proteins lead to MMAF in mice, these include CEP131 [40] and CCDC42 [41]. The discovery that MMAF in humans is linked to CCDC146, known so far as a centrosomal protein, adds to our knowledge of proteins important for axoneme biogenesis.

In this manuscript, we first evaluated the localization of endogenous CCDC146 during the cell cycle in two types of cell cultures, immortalized cells and primary human foreskin fibroblasts. To validate the gene candidate and improve our knowledge of the corresponding protein, we also generated two mouse models. The first one was a *Ccdc146* KO model, with which to study the impact of lack of the protein on the general phenotype, and in particular on male reproductive function using several optical and electronic microscopy techniques. The second model was a HA-tagged CCDC146 model, with which we studied the localization of the protein in different cell types. Data from these genetically modified mouse models were confirmed in human sperm cells.

151 ## Results

152 **1/ WES identifies *CCDC146* as a gene involved in MMAF**

153 We performed whole exome sequencing (WES) to investigate a highly-selected cohort of 167 MMAF
154 patients previously described in [9]. The WES data was analyzed using an open-source bioinformatics
155 pipeline developed in-house, as previously described [42]. From these data, we identified two patients
156 with homozygous truncating variants in the *CCDC146* (coiled-coil domain containing 146) gene,
157 NM_020879.3 (Figure 1A). No other candidate variants reported to be associated with male infertility
158 was detected in these patients. This gene is highly transcribed in both human and mouse testes (Supp
159 Figure 1). The first identified mutation is located in exon 9/19 and corresponds to c.1084C>T, the
160 second is located in exon 15/19 and corresponds to c.2112Del (Figure 1B). The c.1084C>T variant is a
161 nonsense mutation, whereas the single-nucleotide deletion c.2112Del is predicted to induce a
162 translational frameshift. Both mutations were predicted to produce premature stop codons:
163 p.(Arg362Ter) and p.(Arg704serfsTer7), respectively, leading either to the complete absence of the
164 protein, or to the production of a truncated and non-functional protein. The two mutations are
165 therefore most-likely deleterious (Figure 1B). Both variants were absent in our control cohort and their
166 minor allele frequencies (MAF), according to the gnomAD v3 database, were 6.984×10^{-5} and 0
167 respectively. The presence of these variants and their homozygous state were verified by Sanger
168 sequencing, as illustrated in Figure 1. Taken together, these elements strongly suggest that mutations
169 in the *CCDC146* gene could be responsible for the infertility of these two patients and the MMAF
170 phenotype.

171 **2/ *Ccdc146* knock-out mouse model confirms that lack of CCDC146 is associated with MMAF**

172 To validate the hypothesis that CCDC146 deficiency leads to MMAF and male infertility, we produced
173 by CRISPR/Cas9 two mouse lines carrying each a frameshift mutation in *Ccdc146*
174 (ENSMUST00000115245). (Supp Figure 2). We analyzed the reproductive phenotype of the edited
175 animals form the F2 generation and found that homozygous males were infertile and reproduced the
176 MMAF phenotype like the two patients carrying the homozygous variants in the orthologous gene.
177 Based on these findings, we restricted our study to a strain with a 4-bp deletion in exon 2
178 (c.164_167delTTCG).

179 The KO mice were viable without apparent defects. The reproductive phenotypes of male and female
180 mice were explored. WT or heterozygous animals and KO females were fertile, whereas KO males were
181 completely infertile (Figure 2A). This infertility is associated with a 90% decrease in epididymal sperm
182 concentration (from ~30- to ~3-million) (Figure 2B) and an almost complete absence of motility (Figure

183 2C). Closer examination revealed sperm morphology to be strongly altered, with a typical MMAF
184 phenotype and marked defects in head morphology (Figure 2E) indicative of significantly impaired
185 spermiogenesis. In addition, testicle weight relative to whole body weight was significantly lower
186 (Figure 2D), suggesting a germ cell rarefaction in the seminiferous epithelia due to high apoptosis level.
187 A study of spermatogenic cell viability by TUNEL assay confirmed this hypothesis, with a significant
188 increase in the number of positive cells in *Ccdc146* KO animals (Supp Figure 3). Comparative
189 histological studies (Figure 3) showed that on sections of spermatogenic tubules, structural and shape
190 defects were present from the elongating spermatid stage in KO mice, with almost complete
191 disappearance of the flagella in the lumen. At the epididymal level, transverse sections of the
192 epididymal tubules from KO males contained almost no spermatozoa, and the tubules were filled with
193 an acellular substance.

194

195 **3/*CCDC146* codes for a centriolar protein**

196 CCDC146 has been described as a centriolar protein in immortalized HeLa cells [28, 29]. To confirm this
197 localization, we performed immunofluorescence experiments (Figure 4). First, we focused on the
198 centrosome. In HEK-293T cells, using an antibody recognizing centrin (anti-centrin Ab) as a centriole
199 marker and an anti-CCDC146 Ab, CCDC146 was shown to colocalize with centrioles. However, the
200 signal was not strictly localized to centrioles, as peri-centriolar labeling was clearly visible. As this
201 labeling pattern suggests the presence of centriolar satellite proteins, we next performed co-labeling
202 with an antibody recognizing PCM1, a canonical centriolar satellite marker [43]. Once again, the
203 colocalization was only partial (Supp Figure 4). Based on these observations, CCDC146 has a unique
204 localization profile that may indicate specific functions.

205

206 **4/ CCDC146 co-localizes with multiple tubulin-based organelles.**

207 Interestingly, our immunofluorescence experiments revealed that CCDC146 labeling was not strictly
208 limited to centrosomes – other tubulin-containing cellular substructures were also labeled, particularly
209 structures emerging during cell division (Figure 5). Thus, the mitotic spindle was labeled at its base and
210 at its ends. The co-labeling intensified in the midzone during chromatid separation. Finally, the
211 separation structure between the two cells, the midbody, was also strongly stained. As HEK-293T cells
212 are an immortalized cell line, we therefore verified that this labeling pattern was not due to an aberrant
213 expression profile and that it also reflected the situation in primary cell lines. Identical labeling profiles
214 were observed in freshly-prepared Human foreskin fibroblasts (HFF cells) (Supp Figure 5).

215

216 **5/ Expression profile of CCDC146 during the first wave of spermatogenesis in mouse**

217 From our immunofluorescence analysis of somatic cell lines, it was clear that CCDC146 expression is
218 associated with the cell cycle. In the testis, a wide variety of cell types co-exist, including both somatic
219 and germline cells. The germline cells can be further subcategorized into a wide variety of cells, some
220 engaged in proliferation (spermatogonia), others in meiosis (spermatocytes), or in differentiation
221 (spermatids). To better understand the role of CCDC146 in spermatogenesis, and thus how its absence
222 leads to sperm death and malformation, we initially studied its expression during the first wave of
223 spermatogenesis [44] and sought to detect the protein in testis extracts at several postnatal timepoints
224 and in the mature epididymal spermatozoon. Results from this study should shed light on when
225 CCDC146 is required for sperm formation. Surprisingly, RT-PCR failed to detect *Ccdc146* transcripts in
226 proliferating spermatogonia on day 9 after birth (Figure 6A). Transcription of *Ccdc146* started on day
227 18, concomitantly with the initiation of meiosis 2. Expression peaked on day 26, during the
228 differentiation of spermatids. We also wished to explore the expression of the protein. To overcome a
229 lack of specific antibodies recognizing mouse CCDC146, a transgenic mouse was created:
230 (hemagglutinin) sequence was inserted by the CRISPR/Cas9 system into the coding sequence of the
231 *Ccdc146* gene between the two first codons to produce a tagged protein at the N-terminus domain
232 (Supp Figure 6). This insertion induced no phenotypic changes, and both female and male mice were
233 viable with normal fertility. Tag insertion was validated by Western blotting (WB) (Figure 6B). The
234 theoretical MW of the tagged protein is around 116.2 kDa (115.1 + 1.1); the observed MW was slightly
235 higher, suggesting some post-translational modifications. Using these mice, testicular extracts from
236 several postnatal timepoints and from epididymal spermatozoa were analyzed (Figure 6B). In
237 accordance with RT-PCR experiments, bands corresponding to HA-tagged CCDC146 were detectable
238 at D26 and 35, and in epididymal sperm (Figure 6C). The protein is therefore present during spermatid
239 differentiation and conserved in mature sperm. The absence of the protein during spermatogonia
240 proliferation suggests a new function for CCDC146 in sperm cells.

241

242 **6/ In sperm, CCDC146 is present in the flagellum, not in the centriole**

243 To attempt to elucidate the function of CCDC146 in sperm cells, we next studied its localization by IF
244 in human and murine spermatozoa. We focused successively on the anterior segment (head, neck and
245 beginning of the intermediate piece) of the sperm and then on the flagellum. In humans, the
246 spermatozoon retains its two centrioles [32], and they are observable in the neck, as shown by anti-

247 centrin and anti-tubulin labeling (Figure 7A1-3). No colocalization of the CCDC146 label with centrin
248 was observed on human sperm centrioles, suggesting that the protein is not present in or around this
249 structure. However, two unexpected labeling events were observed: sub-acrosomal labeling and
250 labeling of the midpiece. At the flagellum level, faint staining was observed along the whole length
251 (Figure 7A4).

252 To enhance resolution, ultrastructure expansion microscopy (U-ExM), an efficient method to study in
253 detail the ultrastructure of organelles [45], was used (Figure 7B). The localization of the two centrioles
254 was perfectly visible following anti-tubulin labeling, and was confirmed by co-labeling with an anti-
255 POC5 Ab (Supp Figure 7). Once again, no CCDC146 labeling was observed on sperm centrioles (Figure
256 7B3), confirming the conventional IF results. Moreover, U-ExM unveiled that the observed CCDC146
257 midpiece staining (Figure 7A) seems in fact associated with isolated structures, which we hypothesize
258 could be mitochondria, now visible by expansion (Figure 7B1). This suggests that the labeling on the
259 midpiece observed in IF corresponds to non-specific mitochondrial labeling. This conclusion is
260 supported by the fact that the same isolated structures were also labeled with anti-POC5 Ab (Supp
261 Figure 7). In contrast, at the flagellum level, clear punctiform labeling was observed along the whole
262 length of the main piece (Figure 7B1-B3), confirming that the protein is present in the sperm flagellum.

263 The same experiments were performed on murine epididymal spermatozoa. For this study, we used
264 the mouse model expressing HA-tagged CCDC146 protein. It should be noted that unlike in humans, in
265 mice, centrioles are no longer present in epididymal spermatozoa [33]. In conventional IF, using an
266 anti-HA Ab, labeling was observed along the whole flagellum (Figure 8A). The strong HA-labeling in the
267 midpiece was clearly non-specific, as the signal was still present when secondary antibodies were used
268 alone (Supp Figure 8). In expansion microscopy, unexpectedly, the mouse flagellum presented breaks
269 that most likely resulted from the expansion procedure (Figure 8B). Interestingly, strong HA-labeling
270 was observed at the level of these breaks suggesting that CCDC146 epitopes are buried inside the
271 axonemal structure and become accessible mostly on blunt or broken microtubule doublets. The same
272 pattern was observed with three different anti-HA antibodies (Figure 8A-C). To confirm the presence
273 of CCDC146 in the flagellum, sperm flagella were purified after mild sonication, and protein extracts
274 were analyzed by WB (Figure 8D). In the flagella fraction, the HA Ab revealed a single band at around
275 120 kDa, thus confirming the flagellar localization of CCDC146 in both human and mouse sperm.

276 **7/ CCDC146 labeling associates with microtubule doublets**

277 We next wanted to determine whether CCDC146 staining was associated with the axoneme or
278 accessory structures of the flagellum (outer dense fibers or fibrous sheath), and if yes, whether it was
279 associated with microtubule doublets or the central pair. To do so, we used U-ExM on human sperm

280 and quantified the relative position of each CCDC146 dot observed (outside the axoneme, outer left
281 and right; microtubule doublets left and right and central pair – Figure 9A-C). The distribution of
282 localizations was summarized in two bar graphs, generated for two distinct sperm cells. Labeling was
283 preferentially located on the right and left doublets (Figure 9D and 9F), indicating that CCDC146
284 associates more with microtubule doublets. Analysis of protein distribution in mice was not easy,
285 because signal tended to concentrate at breaks. Nevertheless, on some spermatozoa with frayed
286 microtubule doublets., i.e. with the flagellum taking on the shape of a hair, we could find that isolated
287 doublets carried the punctiform labeling confirming the results of analyses on human spermatozoa
288 (Figure 9G). Taken together, these results from mouse and human sperm demonstrate that CCDC146
289 is an axonemal protein, probably associated with microtubule doublets.

290 **8/ CCDC146 could be a Microtubule Inner Protein (MIP)**

291 The presence of extensive labeling at axoneme breaks suggests that the antigenic site is difficult to
292 access in an intact flagellum. We therefore hypothesized that CCDC146 could be a MIP. MIPs are
293 generally resistant to solubilization by detergents. However, N-lauroylsarcosine (sarkosyl) can
294 solubilize microtubule doublets, with increasing concentrations destabilizing first the A-tubule, then
295 the B-tubule [46, 47]. Microtubule solubilization allows release of the MIPs contained within the
296 tubules, and the method is recognized [48, 49]. To test whether our hypothesis that CCDC146 is a MIP,
297 we treated spermatozoa from HA-tagged CCDC146 mice with sarkosyl and performed a WB on the
298 supernatant (Figure 10A). The protein was effectively solubilized, leading to the appearance of bands
299 at around 120 kDa on an SDS-PAGE gel following migration of extracts from sperm treated with 0.2
300 and 0.4% sarkosyl concentrations. Interestingly, a second band around 90 kDa was also
301 immunodecorated by anti-HA antibody in the sarkosyl treated sample, a band not present in the
302 protein extracts from WT males. The other detergents and buffers tested – RIPA, CHAPS or Tris-HCl –
303 barely solubilized CCDC146 or led to no solubilization (Figure 10B). This result confirms the unique
304 action of sarkosyl on CCDC146 and strengthens the hypothesis that the protein is localized in the lumen
305 of tubules. To confirm the action of sarkosyl on the accessibility of the antigenic site, murine
306 spermatozoa were labeled with an anti-HA antibody after treatment with sarkosyl or no treatment.
307 CCDC146 labeling was significantly increased in the presence of sarkosyl (Figure 10C). The full image
308 panel including secondary Ab control experiments can be found in Supp Figure 9.

309 **9/ KO models show defects in tubulin-made organelles**

310 To better characterize the function of CCDC146 in mouse sperm, we went on to perform a detailed
311 morphological analysis of tubulin-made organelles by IF, and examined the morphological defects
312 induced by the absence of CCDC146 at the subcellular level by scanning and/or transmission electron

313 microscopy. This work was performed on immature testicular sperm and on seminiferous tubule
314 sections from adult WT and KO males. Mouse testicular sperm were used because they still contain
315 centrioles that become disassembled as sperm transit through the epididymis [50]. We mainly focused
316 our analyses on the centrioles, the manchette, and the axoneme.

317 The connecting piece between the head and the flagellum, known as the sperm head-tail coupling
318 apparatus (HTCA), is a complex structure containing several substructures including both centrioles,
319 the capitulum and the segmented columns. The distal centriole is embedded in the segmented column
320 and the axoneme emerges from the distal centriole. This structure has a specific shape when observed
321 by scanning electron microscopy (Figure 11A). In *Ccdc146* KO sperm, the connecting piece was severely
322 damaged (Figure 11A). In WT testicular sperm, IF experiments show that the centrioles, identified by
323 anti-tubulin Ab, are very close to each other and adjacent to the capitulum (Figure 11B). In *Ccdc146*
324 KO males, centriole separation was visible in numerous spermatozoa (Figure 11B3, B4), with the
325 structures located far away from the connecting piece (Figure 11B5) or duplicated (Figure 11B6).
326 Interestingly, the overall structure of the HTCA under construction in spermatids, observed by TEM,
327 was conserved in *Ccdc146* KO spermatids, with the presence of both centrioles, containing nine triplets
328 of microtubules, the proximal centriole and its adjunct, as well as accessory cytoskeletal structures,
329 including the capitulum and the segmented columns (Figure 12AB). Remarkably, in a very large
330 proportion of sections, no singlet or doublet of microtubules emerged from the distal KO centriole,
331 suggesting that the process of tubulin polymerization is somehow hampered in these cells (Figure 12A).
332 The absence of microtubules at the end of the distal centriole was confirmed by analysis of serial
333 sections of the sperm centrioles (Figure 12C). Moreover, the defects observed in IF experiments, such
334 as duplication, or defective attachment to the nuclear membrane, were frequently confirmed in TEM
335 images (supp Figure 10). Such defects were not observed in WT spermatids.

336 Manchette formation – which occurs from the round spermatid to fully-elongated spermatid stages –
337 was next studied by IF using β-tubulin Ab. Simultaneously, we monitored formation of the acrosome
338 using an antibody binding to DPY19L2 (Figure 13). Initial acrosome binding at step III was not disrupted,
339 and we observed no differences in the caudal descent of the acrosome during subsequent steps (III-
340 VIII). The development of the manchette in between stages IX-XII was not hampered, but noticeable
341 defects appeared indicating defective manchette organization– such as a random orientation of the
342 spermatids and abnormal acrosome shapes. Finally, at step I, the manchette was clearly longer and
343 wider than in WT cells, suggesting that the control of the manchette biogenesis is defective. In TEM,
344 microtubules in the manchette were clearly visible surrounding the compacting nucleus of elongating
345 spermatids. However, many defects such as marked asymmetry and enlargement were visible (Figure
346 14). The manchette normally anchors on the perinuclear ring, which is itself localized just below the

347 marginal edge of the acrosome and separated by the groove belt [51]. In KO spermatids, the
348 perinuclear ring was no longer localized in the vicinity of the acrosome and was often spread into the
349 cytoplasm, providing a large nucleation structure for the manchette (Figure 14 D-F, red arrows), which
350 explains its width and irregularity.

351 Numerous defects were also observed in the axoneme. These axoneme defects were generally similar
352 to the defects observed in other MMAF mouse models, with disorganization of the axoneme structure
353 (Figure 15A) accompanied by fragmentation of the dense fibers and their random arrangement in cell
354 masses anchored to the sperm head (Figure 15C). The absence of emerging singlet or doublet
355 microtubules at the base of the distal centriole leads to a complete disorganization of the flagellum
356 and the presence of notably dense fiber rings devoid of internal tubulin elements (Figure 15BC).

357 Finally, the shape of the nucleus presented numerous abnormalities (Supp Figure 11). The emergence
358 of head defects was concomitant to the implantation of the manchette, with no defects observed on
359 round spermatids at stages III-VIII. Unexpectedly, a distortion was created in the center of the nucleus
360 at the anterior pole, causing the formation of a bilobed compacted nucleus (Supp Figure 13E-G)
361 containing visible vacuoles.

362

363

364 ## Discussion

365 This study allowed us to identify and validate the involvement of a new candidate gene in male
366 infertility, *CCDC146*. This gene was first described in mice by our team earlier this year, in the context
367 of a research project on the different types of genetic causes of sperm abnormalities in mouse [52].
368 However, no data other than the sperm phenotype (MMAF) was presented in this initial report. In this
369 paper, we present for the first time, the evidence of the presence of mutations in humans and a
370 description of the localization of the protein in somatic and germ cells. We also examined the lesion
371 spectrum at the subcellular level, to obtain a detailed view of the molecular pathogenesis associated
372 with defects in this gene.

373 **1/ Genetic complexity of MMAF**

374 It is essential to characterize all genes involved in male infertility. Therefore, the characterization of a
375 new gene involved in MMAF syndrome is not just "one more gene". First, it further confirms that
376 MMAF syndrome is a heterogeneous recessive genetic disease, currently associated with defects in
377 more than 50 genes. Second, it helps direct the diagnostic strategy to be directed during genome-wide
378 searches. The type of profiling required for MMAF is very different from that performed for instance
379 for cystic fibrosis, where one mutation is responsible for more than 50% of cases. Third, the discovery
380 of all genes involved in MMAF is important in the context of oligogenic heterozygous inheritance of
381 sperm abnormalities in human [52]. Indeed, a homozygous deleterious mutation is found in only half
382 of all MMAF patients, suggesting that other modes of inheritance must be involved. Only by
383 establishing an extended list of genes linked to MMAF will it be possible to determine whether
384 oligogenic heterozygous inheritance is a relevant cause of this syndrome in humans. Finally, some of
385 the genes involved in MMAF syndrome are also involved in ciliary diseases [7]. By further exploring
386 MMAF-type infertility, we can hope to enhance our understanding of another underlying pathology.
387 Although the vast majority of patients with PCD are diagnosed before 5 years of age [53], one study
388 showed that in a in a cohort of 240 adults with a mean age of 36 years (36 ± 13) presenting with chronic
389 productive cough and recurrent chest infections, PCD was identified for the first time in 10% of patients
390 [54]. This result suggests that infertility diagnosis can occur before PCD diagnosis, and consequently
391 that infertility management might improve PCD diagnosis and care.

392 **2/ Functional complexity of CCDC146**

393 The results presented in this report show striking differences in localization of CCDC146 between
394 somatic and germ cells. Our results show that the protein displays several subcellular localizations,
395 which vary according to the cell cycle, and the cell nature. In somatic cells, the protein is mostly

396 associated with the centrosome and other microtubular structures – in particular the mitotic spindle –
397 at the end of microtubules and at the level of the kinetochore and the midbody. These observations
398 identify CCDC146 as a microtubule-associated protein (MAP). In contrast, in spermatozoa, IF images
399 indicate that CCDC146 is an axonemal protein that could be localized in the microtubule doublets.
400 Moreover, the CCDC146 signal was enhanced when sperm were treated with the sarkosyl detergent,
401 used to identify microtubule inner proteins (MIP). Finally, expansion microscopy revealed a strong
402 signal in mouse sperm at the point of axoneme rupture. Taken together, these elements suggest that
403 CCDC146 may be a MIP. Despite its broad cellular distribution, the association of CCDC146 with
404 tubulin-dependent structures is remarkable. However, centrosomal and axonemal localizations in
405 somatic and germ cells, respectively, have also been reported for CFAP58 [37, 55], thus the re-use of
406 centrosomal proteins in the sperm flagellar axoneme is not unheard of. In addition, 80% of all proteins
407 identified as centrosomal are found in multiple localizations
408 (https://www.proteinatlas.org/humanproteome/subcellular/centrosome). The ability of a protein to
409 home to several locations depending on its cellular environment has been widely described, in
410 particular for MAP. The different localizations are linked to the presence of distinct binding sites on
411 the protein. For example, MAP6 binds and stabilizes microtubules, through Mc modules, and
412 associates with membranes and neuroreceptors through palmitoylated cysteines. MAP6 can also
413 localize in the microtubule lumen, in its role as MIP, thanks to its Mn modules. Finally, in addition to
414 its associations with subcellular compartments and receptors, the presence of proline-rich domains
415 (PRD) in the MAP6 sequence, allows it to bind to SH3-domain-containing proteins, and thus triggering
416 activation of signaling pathways [56]. Another example of a protein with multiple localizations is
417 CFAP21, which is a MIP but also a cytosolic calcium sensor. In the latter capacity, CFAP21 modulates
418 the interaction of STIM1 and ORAI1 upon depletion of calcium stores [57, 58]. These examples
419 illustrate the complexity of function of some multiple-domain proteins.

420 The fact that CCDC146 can localize to multiple subcellular compartments suggests that it also contains
421 several domains. Interestingly, a PF05557 motif (Pfam mitotic checkpoint protein,
422 https://www.ebi.ac.uk/interpro/protein/UniProt/E9Q9F7/) has been identified in the mouse CCDC146
423 sequence between amino acids 130 and 162. Proteins belonging to the "mitotic spindle checkpoint"
424 monitor correct attachment of the bipolar spindle to the kinetochores. The presence of this motif likely
425 explains the ability of CCDC146 to localize to cell cycle-dependent subcellular compartments
426 containing tubulin. However, the most important structural motifs identified in CCDC146 are the
427 coiled-coil domains. Although coiled-coils play a structural role in a variety of protein interactions, their
428 presence in CCDC146 remains mysterious, and how they contribute to its function remains to be
429 elucidated. Nevertheless, this motif is compatible with a MIP function for this protein, since several

430 MIP proteins including CCDC11 (FAP53), CCDC19 (FAP45), and CCDC173 (FAP210) are coiled-coil
431 proteins [57]. It is worth noting that the ortholog of *CCDC146* in *Chlamydomonas*, *MBO2*, codes for a
432 protein required for the beak-like projections of doublets 5 and 6, located inside the lumen of the
433 tubule B [59], in the proximal part of the *Chlamydomonas* flagellum. Although no beak-like projections
434 are present in the mammalian axoneme, the location inside the tubule seems to be evolutionarily
435 conserved. A more recent study of MBO2 showed that the protein is also present all along the flagellum
436 of *Chlamydomonas* and is tightly associated with microtubule doublets [60]. These observations
437 support our results showing association of CCDC146 with this axonemal structure.

438 The results presented here also show a striking difference in the phenotype induced by the lack of the
439 protein in somatic and male germ cells. This protein is essential for spermatogenesis, and its absence
440 leads to immotile non-functional sperm and to complete infertility in both humans and mice.
441 Conversely, both patients and *Ccdc146* KO mice seem to be healthy and present no other conditions
442 such as primary ciliary dyskinesia (PCD). CCDC146, despite its wide expression profile in many tissues
443 therefore seems to be dispensable except during spermatogenesis. Nevertheless, because this protein
444 is localized on the tips of the spindle and may be involved in mitotic checkpoints, its absence may lead
445 to late proliferative disorders. This hypothesis is supported by the fact that *CCDC146* is reported to be
446 down-regulated in thyroid cancer [61]. The link between infertility and risk of cancer was recently
447 underlined, with mutations found in genes like *FANCM* [62]. Therefore, it would be interesting to
448 monitor aging in *Ccdc146* KO mice and to study their life expectancy and cancer rates compared to WT
449 mice.

450 **3/ Absence of CCDC146 in sperm centriole**

451 Several proteomics studies of the sperm centriole identified CCDC146 as a centrosome-associated
452 protein in bovine sperm [28, 63], a species where centrioles are present in ejaculated sperm. Using a
453 different methodological approach, based on IF with conventional and expansion microscopy, we
454 observed no CCDC146 signal in centrioles from testicular mouse and ejaculated human sperm. The
455 same result was obtained with two different types of antibodies: with human sperm, we used a
456 commercial anti-CCDC146 Ab, whereas with mouse sperm we used several anti-HA antibodies. The
457 same IF approach allowed us to clearly identify the sperm centrosome using a number of antibodies
458 such as anti-POC5 and anti-beta tubulin, ruling out a possible failure of our IF protocol. It is worth
459 noting that centrosomal proteins were isolated from whole flagella using several strategies including
460 sequential use of multiple detergents, and that the centrosomal proteins were purified in the last
461 fractions. These results indicate that CCDC146 is in fact barely soluble in conventional buffers, which
462 could explain why it is co-purified with the centrosomal fraction in proteomics studies.

463 **4/ TEM reveals that lack of CCDC146 severely impacts microtubule-based organelles**

464 No morphological defects were observed before the elongating spermatid stage, and in round
465 spermatids, the acrosome started to spread on the nucleus in a normal way (Figure 13). Morphological
466 defects appeared clearly from the onset of spermatid elongation. This result indicates that the protein
467 is only necessary for late spermiogenesis, from the phase corresponding to flagellum biogenesis. All
468 the organelles composed mainly of tubulin were strongly affected by the absence of the protein.

469 The manchette structure in elongating *Ccdc146* KO spermatids was asymmetric, abnormally broad,
470 and ectopic, leading to the formation of aberrantly-shaped sperm heads. So far, manchette defects
471 have been associated with defects in intra-flagellar transport (IFT), and intra-manchette transport
472 (IMT) [64]. CCDC146 was only localized to the sperm axoneme by IF, and no signal was observed in the
473 manchette, suggesting that CCDC146 is probably not involved in the transport machinery. Moreover,
474 our results indicated that the manchette was remarkably long in elongated spermatids. A similar
475 phenotype was observed in Katanin80-deficient animals [65]. Katanin80 is a microtubule-severing
476 enzyme that is important for manchette reduction. Interestingly, the absence of WDR62, a scaffold
477 protein involved in centriole duplication, leads to defective katanin80 expression, and the presence of
478 elongated manchettes in mice [66]. In combination with our results, this detail suggests that the
479 manchette's structure and its reduction are influenced by centrosomal proteins, possibly through
480 katanin defects. The precise molecular link between CCDC146 and manchette assembly and reduction
481 remains to be identified.

482 The HTCA was also aberrant in *Ccdc146* KO spermatids. Centrioles in elongating spermatids were
483 frequently displaced from their implantation fossa at the nuclear envelope. We observed some
484 correctly lodged centrioles in round spermatids; however, we are unable to determine with certainty
485 whether the majority of centrioles failed to correctly attach or whether they detached from the nuclear
486 envelope during spermatid elongation. Defects in cohesion of the HTCA have been associated with the
487 acephalic spermatozoa syndrome, and were shown to involve a number of proteins such as SUN5,
488 SPATA6 and ODF1 [4, 67-69]. Here, we did not observe any sperm decapitation, suggesting that
489 CCDC146 is involved in a different pathway controlling the HTCA. Moreover, elongating *Ccdc146* KO
490 spermatids displayed supernumerary centrioles. Abnormal centriole numbers have also been reported
491 in the absence of a few other centrosome-associated proteins including DZIP1 [36] and CCDC42 [41],
492 and of microtubule-regulating proteins such as katanin like-2 [70] and tubulin deglutamylase CCP5
493 [71].

494 Studies of the spermiogenesis defects observed in different models deficient for centrosomal proteins
495 show some common features such as abnormal manchette and duplicated centrosomes. The absence

496 of these proteins does not appear to be directly responsible for these defects, rather it seems to modify
497 the expression of microtubule regulatory proteins such as katanins [65, 66, 70]. These modifications
498 could explain the pleiotropic effect of the absence of CCDC146 on microtubule-based organelles.

499 In conclusion, by characterizing the genetic causes of human infertility, we not only improve
500 the diagnosis and prognosis of these pathologies but also pave the way for the discovery of new players
501 in spermatogenesis. We are constantly adding to the number of proteins present in the flagella of the
502 mammalian spermatozoa that are necessary for its construction and functioning. This study showed
503 that CCDC146, a protein previously described as a centrosomal protein in somatic and germ cells,
504 localizes in spermatozoa's axonemal microtubule doublets. The presence of CCDC146 in somatic cells'
505 centrosomes gives weight to the idea of a centrosome with a dynamic composition, allowing it to fulfill
506 its multitude of functions throughout all the phases of cellular life.

507

508 ## Material and methods

509 Human subjects and controls

510 We analyzed WES data from a cohort of 167 MMAF individuals previously established by our team [9].
511 All individuals presented with a typical MMAF phenotype characterized by severe asthenozoospermia
512 (total sperm motility below 10%) with at least three of the following flagellar abnormalities present in
513 >5% of the spermatozoa: short, absent, coiled, bent or irregular flagella. All individuals had a normal
514 somatic karyotype (46,XY) with normal bilateral testicular size, normal hormone levels and secondary
515 sexual characteristics. Sperm analyses were carried out in the source laboratories during routine
516 biological examination of the individuals according to World Health Organization (WHO) guidelines
517 [72]. Informed and written consents were obtained from all the individuals participating in the study
518 and institutional approval was given by the local medical ethical committee (CHU Grenoble Alpes
519 institutional review board). Samples were stored in the Fertithèque collection declared to the French
520 Ministry of health (DC-2015-2580) and the French Data Protection Authority (DR-2016-392).

521 Sanger sequencing

522 *CCDC146* single nucleotide variants identified by exome sequencing were validated by Sanger
523 sequencing as previously described [9]. PCR primers used for each individual are listed in Table
524 supplementary 1.

525

526 Cell culture

527 HEK-293T (Human Embryonic Kidney) and HFF (Human Foreskin Fibroblasts) cells were grown in D10
528 consisting in DMEM with GlutaMAX (Dulbecco's Modified Eagle's Medium, Sigma Aldrich)
529 supplemented with 10% heat-inactivated fetal bovine serum (FBS, Life Technologies) and 10% of
530 penicillin-streptomycin (Sigma Aldrich) in a 5% CO_2 humidified atmosphere at 37 °C. HEK-293T cells
531 were divided twice weekly by 1/10 dilution. HFFs cells were divided 1/5 one time a week.

532 Ethics statement

533 Breeding and experimental procedures were carried out in accordance with national and international
534 laws relating to laboratory animal welfare and experimentation (EEC Council Directive 2010/63/EU,
535 September 2010). Experiments were performed under the supervision of C.L. (agreement 38 10 38) in
536 the Plateforme de Haute Technologie Animale (PHTA) animal care facility (agreement
537 C3851610006 delivered by the Direction Départementale de la Protection des Populations) and were

538 approved by the ethics committee of the PHTA and by the French government (APAFIS#7128-
539 2016100609382341.v2).

540 Generation of *Ccdc146* KO and *HA-tagged CCDC146* mice

541 *Ccdc146* KO mice were generated using the CRISPR/Cas9 technology as previously described [52].
542 Briefly, to maximize the chances of generating deleterious mutations, two gRNAs located in two
543 distinct coding exons located at the beginning of the targeted gene were used. For each gene, the two
544 gRNAs (5'-CCT ACA GTT AAC ATT CGG G-3' and 5'-GGG AGT ACA ATA TTC AGT AC-3'), respectively
545 targeting exons 2 and 4, were inserted into two distinct plasmids, each plasmid also contained the Cas9
546 sequence (Supp Figure 2). The Cas9 gene was controlled by a CMV promoter and the gRNA and its RNA
547 scaffold by a U6 promoter. Full plasmids (pSpCas9 BB-2A-GFP (PX458)) containing the specific sgRNA
548 were ordered from Genescript (https://www.genscript.com/crispr-synthetic-sgrna.html). Both
549 plasmids were co-injected into the zygotes' pronuclei at a concentration of 2.5 ng/mL. Plasmids were
550 directly injected as delivered by the supplier, without in vitro production and purification of Cas9
551 proteins and sgRNA.

552 Ccdc146-HA knock-in mice were also generated by CRISPR/Cas9. Twenty-seven nucleotides encoding
553 the HA (hemagglutinin) tag (5'-TAC CCA TAC GAT GTT CCA GAT TAC GCT TAG-3') were inserted
554 immediately after the start codon of Ccdc146. One plasmid containing one sgRNA (5'-TAC TTT AGA ACT
555 GTG AAA AA-3') and Cas9 was injected (5 ng/µL) with a single-stranded DNA (150 nucleotides, 50 ng/µl)
556 as a template for the homology directed repair (HDR) Appendix figure 6. PCR primers used for
557 genotyping are listed in Table supplementary 1. Transgenic CCDC146 strains were bred in the Grenoble
558 university animal platform (HTAG) and housed under specific-pathogen-free conditions. Animals were
559 euthanized by cervical dislocation at the indicated ages.

560

561 Phenotypic analysis of *Ccdc146* KO mice

562 Fertility test – Three adult males of each genotype were housed individually with two fertile
563 WT B6D2 females for 12 weeks. The date of birth and the number of pups were recorded.

564 Sperm analysis – Epididymal sperm were obtained by making small incisions in the mouse
565 caudae epididymides placed in 1 mL of warm M2 medium (Sigma Aldrich), and the sperm were allowed
566 to swim up for 10 min at 37 °C. Sperm samples (10 µL) were used for Computer-assisted semen analysis
567 (CASA, Hamilton Thorn Research, Beverley, MA, USA) using a 100-µm-deep analysis chamber (Leja
568 Products B.V., Nieuw-Vennep, the Netherlands). A minimum of 100 motile sperm was recorded in each
569 assay. The remaining sperm samples were washed in 1X phosphate buffered saline (PBS, Life
570 technologies), 10 µL were spread onto slides pre-coated with 0.1% poly-L-lysine (Epredia), fixed in 70%

571 ethanol (Sigma Aldrich) for 1 h at room temperature (RT) and submitted to a papanicolaou staining
572 (WHO laboratory manual) to assess sperm morphology. Images were obtained using a Zeiss AxioImager
573 M2 fitted with a 40X objective (color camera AxioCam MRc) and analyzed using ZEN (Carl Zeiss, version
574 3.4).

575

576 Testis and epididymides histology

577 Testis and epididymides samples from 8-16-week-old mice were fixed for 24 h in PBS/4% PFA
578 (Electron Microscopy Sciences), dehydrated in a graded ethanol series, embedded in paraffin wax,
579 sectioned at 5 µm and placed onto Superfrost slides (Fischer scientific). For both, slides were
580 deparaffinated and rehydrated prior to use. Tissue morphology and structure were observed after
581 coloration by Mayer's hematoxylin and eosin phloxine B (WHO protocols) using a Zeiss AxioImager M2
582 (color camera AxioCam MRc).

583 Terminal deoxynucleotidyl transferase dUTP nick-end labeling (TUNEL) assay on testes

584 Testes samples from three adult individuals for each genotype were analyzed. Apoptotic cells
585 in testis sections were identified using the Click-iT™ Plus TUNEL Assay kit (Invitrogen) in line with the
586 manufacturer's instructions. DNA strand breaks for the positive control were induced by DNase I
587 treatment. Each slide contained up to eight testis sections. DNA was stained with Hoechst (2 µg/mL).
588 Images were acquired and reconstituted using a Zeiss Axioscan Z1 slide scanner and analyzed by Fiji
589 [73]. The total number of seminiferous tubules and the number of tubules containing at least one
590 TUNEL-positive cell were counted in each testis section.

591 Conventional Immunofluorescence (IF)

592 Somatic Cells – HEK-293T or HFFs (10 000 cells) were grown on 10-mm coverslips previously
593 coated with poly-D-lysine (0.1 mg/mL, 1 h, 37 °C, Gibco) placed in a well on a 24-well plate. After 24 h,
594 cells were directly fixed with ice-cold methanol (Sigma Aldrich) for 10 min. After washing twice in PBS,
595 non-specific sites were blocked with PBS/5% FBS/5% NGS (normal goat serum, Life technologies) for
596 1 h at RT. After washing three times in PBS/1% FBS, primary antibody was added in PBS/1% FBS and
597 incubated overnight at 4 °C. Coverslips were washed three times in PBS/1% FBS before adding
598 secondary antibody in PBS/1% FBS and incubating for 2 h at RT. After washing three times in PBS, nuclei
599 were stained with 2 µg/mL Hoechst 33342 in PBS (Sigma Aldrich). Coverslips were once again washed
600 three times in PBS, then carefully placed on Superfrost slides (cells facing the slide) and sealed with
601 nail polish.

602 Spermatogenic cells – Seminiferous tubules were isolated from mouse testes (8–16 weeks old).
603 After removing of the tunica albuginea, the testes were incubated at 37 °C for 1 h in 3 mL of a solution
604 containing (mM): NaCl (150), KCl (5), CaCl2 (2), MgCl2 (1), NaH2PO4 (1), $NaHCO_3$ (12), D-glucose (11),
605 Na-lactate (6), HEPES (10) pH 7.4, and collagenase type IA (1 mg/mL – Sigma Aldrich). Tubules were
606 rinsed twice in collagenase-free medium and cut into 2-mm sections. Spermatogenic cells were
607 obtained by manual trituration and filtered through a 100-µm filter. The isolated cells were centrifuged
608 (10 min, 500 g), resuspended in 500 µL PBS and 50 µL was spread onto slides pre-coated with 0.1%
609 poly-L-lysine (Epredia) and allowed to dry. Dried samples were fixed for 5 min in PBS/4% PFA. After
610 washing twice in PBS, slides were placed in PBS/0.1% Triton/5% BSA (Euromedex) for 90 min at RT.
611 Following two washes in PBS, the primary antibody was added in PBS/1% BSA overnight at 4 °C. After
612 washing three times in PBS/1% BSA, secondary antibody was added in PBS/1% BSA for 2 h at RT. After
613 washing three times in PBS, nuclei were stained with 2 µg/mL Hoechst 33342 in PBS (Sigma Aldrich)
614 and slides were mounted with DAKO mounting media (Agilent).

615 Testis sections – After deparaffination and rehydration, testis sections were subjected to heat
616 antigen retrieval for 20 min at 95 °C in a citrate-based solution at pH 6.0 (VectorLabs). Tissues were
617 then permeabilized in PBS/0.1% Triton X-100 for 20 min at RT. After washing three times in PBS (5 min
618 each), slides were incubated with blocking solution (PBS/10% BSA) for 30 min at RT. Following three
619 washes in PBS, slides were incubated with primary antibodies in PBS/0.1% Tween/5% BSA overnight
620 at 4 °C. Slides were washed three times in PBS before applying secondary antibodies in blocking
621 solution and incubating for 2 h at RT. After washing in PBS, nuclei were stained with 2 µg/mL Hoechst
622 33342 in PBS (Sigma Aldrich) for 5 min at RT. Slides were washed once again in PBS before mounting
623 with DAKO mounting media (Agilent).

624 Spermatozoa (conventional protocol) - Mouse spermatozoa were recovered from the caudae
625 epididymides. After their incision, sperm were allowed to swim in 1 mL of PBS for 10 min at 37 °C. They
626 were washed twice with 1 mL of PBS 1X at 500 g for 5 min, and 10 µL of each sample was smeared
627 onto slides pre-coated with 0.1% poly-L-lysine (Epredia). Sperm were fixed in PBS/4% PFA for 45 s,
628 washed twice in PBS and permeabilized in PBS/0.1% Triton for 15 min at RT. After incubation in
629 PBS/0.1% Triton/2% NGS for 2 h at RT, primary antibody was added in PBS/0.1% Triton/2% NGS
630 overnight at 4 °C. After washing three times in PBS/0.1% Triton, the secondary antibody was applied
631 in PBS/0.1% Triton/2% NGS for 90 min at RT. Slides were washed three times in PBS before staining
632 nuclei with 2 µg/mL Hoechst 33342 in PBS (Sigma Aldrich). Slides were washed once in PBS before
633 mounting with DAKO mounting media (Agilent).

634 For human spermatozoa, the protocol was based on that of Fishman *et al.* [32]. Straws were
635 thawed at RT for 10 min and resuspended in PBS. Sperm were washed twice in 1 mL of PBS (10 min,
636 400 g), 50 µL was spread onto slides pre-coated with 0.1% poly-L-lysine and left to dry. Dry slides were
637 fixed in 100% ice-cold methanol for 2 min and washed twice in PBS. Cells were permeabilized in PBS/3%
638 Triton X-100 (PBS-Tx) for 1 h at RT. Slides were then placed in PBS-Tx/1% BSA (PBS-Tx-B) for 30 min at
639 RT. Immunofluorescence was performed as for mouse spermatozoa. Sperm were then incubated with
640 primary antibodies in PBS-Tx-B overnight at 4 °C. After washing three times in PBS-Tx-B for 5 min each,
641 slides were incubated with secondary antibodies for 1 h at RT in PBS-Tx-B. After washing three times
642 in PBS, nuclei were stained with 2 µg/mL Hoechst 33342 in PBS (Sigma Aldrich) and slides were
643 mounted with DAKO mounting media (Agilent).

644 Spermatozoa (sarkosyl protocol) - Mouse sperm from caudae epididymides or human sperm
645 from 250-µL straws were collected in 1 mL PBS 1X, washed by centrifugation for 5 min at 500 g and
646 then resuspended in 1 mL PBS 1X. Sperm cells were spread onto slides pre-coated with 0.1% poly-L-
647 lysine (Epredia), treated or not for 5 min with 0.2% sarkosyl (Sigma) in Tris-HCl 1 mM, pH7.5 at RT and
648 then fixed in PBS/4% PFA for 45 s at RT. After washing twice for 5 min with PBS, sperm were
649 permeabilized with PBS/0.1% Triton X-100 (Sigma Aldrich) for 15 min at RT and unspecific sites were
650 blocked with PBS/0.1% Triton X-100/2% NGS for 30 min at RT. Then, sperm were incubated overnight
651 at 4 °C with primary antibodies diluted in PBS/0.1% Triton X-100/2% NGS. Slides were washed three
652 times with PBS/0.1% Triton X-100 before incubating with secondary antibody diluted in PBS/0.1%
653 Triton X-100/2% NGS for 90 min at RT. Finally, sperm were washed three times in PBS/0.1% Triton X-
654 100, adding 2 µg/mL Hoechst 33342 (Sigma Aldrich) during the last wash to counterstain nuclei. Slides
655 were mounted with DAKO mounting media (Agilent). Confocal microscopy was performed on a Zeiss
656 LSM 710 or NIKON eclipse A1R/Ti2 using a 63x oil objective.

657 Image acquisition – For all immunofluorescence experiments, images were acquired using a
658 63X oil objective on a multimodal confocal Zeiss LSM 710 or Zeiss AxioObserver Z1 equipped with
659 ApoTome and AxioCam MRm. Images were processed using Fiji [73] and Zeiss ZEN (Carl Zeiss, version
660 3.4). Figures for cultured cells were arranged using QuickFigures [74].

661 Expansion microscopy (U-ExM)

662 Coverslips used for either sample loading (12 mm) or image acquisition (24 mm) were first
663 washed with absolute ethanol and dried. They were then coated with poly-D-lysine (0.1 mg/mL) for
664 1 h at 37 °C and washed three times with ddH2O before use. Sperm from cauda epididymides or human
665 sperm from straws were washed twice in PBS. $1x10^6$ sperm cells were spun onto 12-mm coverslips for
666 3 min at 300 g. Crosslinking was performed in 1 mL of PBS/1.4% formaldehyde/2% acrylamide

667 (ThermoFisher) for 5 h at 37 °C in a wet incubator. Cells were embedded in a gel by placing a 35-µL
668 drop of a monomer solution consisting of PBS/19% sodium acrylate/10% acrylamide/0.1% N,N'-
669 methylenbisacrylamide/0.2% TEMED/0.2% APS (ThermoFisher) on parafilm and carefully placing
670 coverslips on the drop, with sperm facing the gelling solution. Gelation proceeded in two steps: 5 min
671 on ice followed by 1 h at 37 °C. Coverslips with attached gels were transferred into a 6-well plate for
672 incubation in 5 mL of denaturation buffer (200 mM SDS, 200 mM NaCl, 50 mM Tris in ddH2O, pH 9) for
673 20 min at RT until gels detached. Then, gels were transferred to a 1.5-mL microtube filled with fresh
674 denaturation buffer and incubated for 90 min at 95 °C. Gels were carefully removed with tweezers and
675 placed in beakers filled with 10 mL ddH2O to cause expansion. The water was exchanged at least twice
676 every 30 min. Finally, gels were incubated in 10 mL of ddH2O overnight at RT. The following day, a 5-
677 mm piece of gel was cut out with a punch. To remove excess water, gels were placed in 10 mL PBS for
678 15 min, the buffer was changed, and incubation repeated once. Subsequently, gels were transferred
679 to a 24-well plate and incubated with 300 µL of primary antibody diluted in PBS/2% BSA at 37 °C for
680 3 h with vigorous shaking. After three washes for 10 min in PBS/0.1% Tween 20 (PBS-T) under agitation,
681 gels were incubated with 300 µL of secondary antibody in PBS/2% BSA at 37 °C for 3 h with vigorous
682 shaking. Finally, gels were washed three times in PBS-T for 10 min with agitation. Hoechst 33342
683 (2 µg/mL) was added during the last wash. The expansion resolution was between 4X and 4.2X
684 depending on sodium acrylate purity. For image acquisition, gels were placed in beakers filled with
685 10 mL ddH2O. Water was exchanged at least twice every 30 min, and then expanded gels were
686 mounted on 24-mm round poly-D-lysine-coated coverslips, placed in a 36-mm metallic chamber for
687 imaging. Confocal microscopy was performed using either a Zeiss LSM 710 using a 63x oil objective or
688 widefield was performed using a Leica THUNDER widefield fluorescence microscope, using a 63x oil
689 objective and small volume computational clearing. (Guichard / Hamel lab, Geneva).

690 *Ccdc146* expression

691 Testis from CCDC146-HA pups were collected at days 9, 18, 26 and 35 after birth and directly
692 cryopreserved at -80 °C before RNA extraction. RNA was extracted as follow. Frozen testes were placed
693 in RLT buffer (Qiagen)/1% β-mercaptoethanol (Sigma), cut in small pieces and lysis performed for
694 30 min at RT. After addition of 10 volumes of TRIzol (5 min, RT, ThermoFisher) and 1 volume of
695 chloroform (2 min, RT, Sigma Aldrich), the aqueous phase was recovered after centrifugation at
696 12 000 g, 15 min, 4 °C. RNA was precipitated by the addition of one volume of isopropanol (Sigma) and
697 of glycogen (20 mg/mL, ThermoFisher) as a carrier, tube was placed overnight at -20 °C. The day after,
698 after centrifugation (15 min, 12 000 g, 4 °C), RNA pellet was washed with ethanol 80%, air-dried and
699 resuspended in 30 µl of ultrapure RNAse free water (Gibco). RNA concentrations were determined by

using the Qubit RNA assay kit (ThermoFisher). 800 ng of total RNA were used to perform the RT step using the iScript cDNA synthesis kit (Bio-Rad) in a total volume of 20 µL. Gene expression was assessed by qPCR (1 µL of undiluted cDNA in a final volume of 20 µL with the appropriate amount of primers, see table 1) using the SsoAdvanced Universal SYBR Green Supermix (Bio-Rad). The qPCR program used was 94 °C 15 min, (94 °C 30 s, 58 °C 30 s, 72 °C 30 s) x40 followed by a melt curve analysis (58 °C 0.05 s, 58–95 °C 0.5-°C increment 2–5 s/step). Gene expression was calculated using the $2^{-\Delta\Delta CT}$ method. Results are expressed relative to *Ccdc146* expression on day 9.

	Forward primer		Reverse primer	
Genes	Sequence	Concentration (nM)	Sequence	Concentration (nM)
Ccdc146	5'-TGCTGCATGACGCCGTGATG-3'	750	5'-GGAGACCTCCGTGGAGAATGCTTC-3'	500
Hprt	5'-CCTAATCATTATGCCGAGGATTTGG-3'	500	5'-TCCCATCTCCTTCATGACATCTCG-3'	250
Actb	5'-CTTCTTTGCAGCTCCTTCGTTGC-3'	250	5'-AGCCGTTGTCGACGACCAGC-3'	250

709 CCDC146 detection by WB

710 Protein extraction from the testis – Testis from pups were recovered at days 9, 18, 26 and 35
711 after birth. After removing the albuginea, they were homogenized in 2X Laemmli buffer (Bio-Rad) using
712 a Dounce homogenizer, and heated at 95 °C for 10 min. The supernatant was recovered after
713 centrifugation (15 000 g, 10 min, 4 °C), 5% β mercapto-ethanol was added (Sigma), and tubes were
714 once again incubated at 95 °C for 10 min. After cooling, the supernatant was stored at -20 °C until use.

715 Protein extraction from sperm head and sperm flagella – Spermatozoa from a CCDC146-HA
716 male (9 weeks old) were isolated from both epididymis in 1 mL PBS and washed twice with PBS by
717 centrifugation at RT (5 min, 500 g). Half of the sperm were incubated with 1X protease inhibitor
718 cocktail (mini Complete EDTA-free tablet, Roche Diagnostic), incubated for 15 min on ice and
719 sonicated. Separated flagella were isolated by centrifugation (600 g, 20 min, 4 °C) in a Percoll gradient.
720 Percoll concentrations used were 100%, 80%, 60%, 34%, 26%, 23%, and sperm flagella were isolated
721 from the 60% fraction. Samples were washed with PBS by centrifugation (500 g, 10 min, 4 °C). Whole
722 sperm or sperm flagella were incubated in 2X Laemmli buffer (Bio-Rad), heated at 95 °C for 10 min and
723 centrifuged (15 000 g, 10 min, 4 °C). The supernatants were incubated with 5% β-mercaptoethanol,
724 boiled (95 °C, 10 min), cooled down and placed at -20 °C until use.
725

726 Proteins extraction from total sperm – CCDC146-HA sperm were recovered from caudae
727 epididymides in 1 mL PBS and washed twice in 1 mL PBS by centrifugation 500 g, 5 min. Lysis was then
728 performed for 2 h at 4 °C on wheel in either Chaps buffer (10 mM Chaps / 10 mM HEPES / 137 mM
729 NaCl / 10% Glycerol), in RIPA Buffer (Pierce IP Lysis buffer, ThermoFisher), in Tris 10 mM / HCl 1 M
730 buffer or in Tris 10 mM / HCl 1 M / 0.2 to 0.8% sarkosyl buffer. After centrifugation 15 000 g, 4 °C,
731 15 min, the supernatants were recovered and 5% of β-mercaptoethanol added. After boiling (95 °C,
732 10 min), the samples were cooled down and placed at -20 °C until use.

733 Western blot – Protein lysates were fractionated on 5-12% SDS-PAGE precast gels (Bio-Rad)
734 and transferred onto Trans-Blot Turbo Mini 0.2 µm PVDF membranes using the Trans-Blot Turbo
735 Transfer System (Bio-Rad) and the appropriate program. Membranes were then blocked in PBS/5%
736 milk/0.1% Tween 20 (PBS-T) for 2 h at RT before incubating with the primary antibody in PBS-T
737 overnight at 4 °C with agitation. Membranes were then washed three times for 5 min in PBS-T and
738 incubated with the secondary HRP-antibody in PBS-T for 1 h at RT. After three washes (PBS-T, 10 min),
739 the membrane was revealed by chemiluminescence using the Clarity ECL substrate (Bio-Rad) and
740 images were acquired on a Chemidoc apparatus (Bio-Rad).

741 Transmission electron microscopy

742 Transmission electron microscopy was performed by Dr. Stefan Geimer at the University of Bayreuth
743 as follows. Testis from adult mice were fixed in PBS/4% paraformaldehyde (PFA). They were then
744 decapsulated from the tunica albuginea and the seminiferous tubules were divided into three to four
745 pieces using a razor blade (Gillette Super Sliver). The seminiferous tubules were incubated for 60 min
746 at RT in fixation buffer (100 mM HEPES pH7.4, 4 mM CaCl2, 2.5% glutaraldehyde, 2% PFA, all from
747 Sigma Aldrich) and then the buffer was exchanged with fresh fixation buffer and the samples left
748 overnight fixed at 4 °C. After washing three times for 10 min in 100 mM HEPES pH 7.4, 4 mM CaCl2,
749 samples were post-fixed in 1% osmium tetroxide (Carl Roth, Karlsruhe, DE) in distilled water for
750 120 min at 4 °C. After three additional 10-min washes in distilled water, the tissue pieces were
751 embedded in 1.5% DifcoTM Agar noble (Becton, Dickinson and Company, Sparks, MD, US) and
752 dehydrated using increasing concentrations of ethanol. The samples were then embedded in glycidyl
753 ether 100 (formerly Epon 812; Serva, Heidelberg, Germany) using propylene oxide as an intermediate
754 solvent according to the standard procedure. Ultrathin sections (60-80 nm) were cut with a diamond
755 knife (type ultra 35°; Diatome, Biel, CH) on the EM UC6 ultramicrotome (Leica Microsystems, Wetzlar,
756 Germany) and mounted on single-slot pioloform-coated copper grids (Plano, Wetzlar, Germany).
757 Finally, sections were stained with uranyl acetate and lead citrate [75]. To obtain different section
758 planes within a sample, serial sections (60-80 nm) were made using the same method. The sectioned
759 and contrasted samples were analyzed under a JEM-2100 transmission electron microscope (JEOL,
760 Tokyo, JP) at an acceleration voltage of 80 kV. Images were acquired using a 4080 x 4080 charge-
761 coupled device camera (UltraScan 4000 - Gatan, Pleasanton, CA, US) and Gatan Digital Micrograph
762 software. The brightness and contrast of images were adjusted using the ImageJ program.

763 Scanning electron microscopy

764 The two epididymides of mature males were recovered in 1 mL of 0.1 M sodium cacodylate buffer (pH
765 7.4, Electron Microscopy Sciences) and the sperm were allowed to swim for 15 min at 37 °C. After
766 centrifugation for 10 min, 400 g, RT, the supernatant was discarded and the pellet resuspended in
767 primary fixating buffer (2% glutaraldehyde/0.1 M sodium cacodylate buffer, pH 7.4, Electron
768 Microscopy Sciences) for 30 min at 4 °C. After washing three times in 0.1 M sodium cacodylate buffer
769 (400 g, 10 min), the pellet was submitted to post fixation using 1% Osmium tetroxide 2% (OsO4,
770 Electron Microscopy Sciences) in 0.1 M sodium cacodylate buffer for 30 min at 4 °C. Fixed cells were
771 washed three times in 0.1 M sodium cacodylate buffer (400 g, 5 min), the sample was then placed on
772 a coverslip and treated with Alcian blue 1% (Electron Microscopy Sciences) to improve attachment.
773 The sample was then dehydrated in graded ethanol series: 50%, 70%, 80%, 90%, 96% and 100%
774 (10 min, once each). Final dehydration was performed for 10 min in a v/v solution of 100%
775 ethanol/100% Hexamethyldisilazane (HMDS) followed by 10 min in 100% HMDS. Samples were left to

776 dry overnight before performing metallization. Samples were analyzed using a Zeiss Ultra 55
777 microscope at the C.M.T.C. – Consortium des Moyens Technologiques Communs (Material
778 characterization platform), Grenoble INP.

779 Statistical analysis

780 The statistics related to the reproductive phenotypes were automatically calculated by GraphPad
781 Prism 8 and 9. Statistical differences were assessed by applying an unpaired t test and one-way ANOVA.
782 Histograms show mean ± standard deviation, and p-values were considered significant when inferior
783 to 0.05.

784 Antibodies used

Primary antibodies				
Target	**Host species**	**Reference**		**Dilution**
CCDC146	Rabbit	Atlas Antibodies	HPA020082	IF: 1/200 U-ExM: 1/200
Centrin, 20H5	Mouse	Merck	04-1624	IF: 1/200
γ-tubulin	Mouse	Santa Cruz Biotechnology	sc-17787	IF: 1/500
β-tubulin	Guinea pig	Geneva Antibody Facility	AA344-GP	IF: 1/500
β-tubulin	Rabbit	Cell Signaling Technology	2128	IF: 1/100
PCM1 (G-6)	Mouse	Santa Cruz Biotechnology	sc-398365	IF: 1/200
α-tubulin	Mouse	Geneva Antibody Facility	AA-345	U-ExM: 1/250
β-tubulin *			AA-344	IF: 1/500
POC5	Rabbit	Bethyl	A303-341A	IF: 1/250 U-ExM: 1/200
High Affinity (HA)	Rat	Roche	11867423001	IF: 1/400

				U-ExM: 1/400 WB: 1/2500
High Affinity (HA)	Rabbit	Cell Signaling Technology	3724	U-ExM: 1/100
High Affinity (HA)	Rabbit	Sigma Aldrich	H6908	U-ExM: 1/200
Dpy19L2	Rabbit	**		IF: 1/100

785

Target	**Fluorophore**	**Reference**		**Dilution**
Goat anti-Rabbit	Alexa Fluor 488	Jackson ImmunoResearch	111-545-144	IF: 1/800 U-ExM: 1/250
Goat anti-Mouse	DyLight 549	Jackson ImmunoResearch	115-505-062	IF: 1/400
Goat anti-Guinea Pig	Alexa Fluor 647	Invitrogen	A-21450	IF: 1/800
Goat anti-Rabbit	Alexa Fluor 568	Life Technologies	A11036	U-ExM: 1/250
Goat anti-Mouse	Alexa Fluor 488	Life Technologies	A11029	U-ExM: 1/250
Goat anti-Rat	Alexa Fluor 549	Jackson ImmunoResearch	112-505-175	IF: 1/800
Goat Anti-Rat	HRP conjugate	Merck	AP136P	1/10 000

786

787 *α-tubulin and β-tubulin were used together and noted as α+β-tubulin

788 **Dpy19l2 antibodies are polyclonal antibodies produced in rabbit that were raised against
789 RSKLREGSSDRPQSSC and CTGQARRRWSAATMEP peptides corresponding to amino acids 6-21 and 21-
790 36 of the N-terminus of mouse Dpy19l2, as described in [76].

791 **Acknowledgments.**

792 This work was supported by INSERM, CNRS, Université Grenoble Alpes, the French Agence Nationale
793 pour la Recherche (ANR) grants ‘‘MAS-Flagella’’ (ANR-19-CE17-0014), and “FLAGELOME” (ANR-19-

CE17-0014) to P.F.R., the Direction Générale de l'Offre de Soin (DGHOS) for the program PRTS 2014 to P.F.R., the Fondation Maladies Rares (FMR)- grant ''Whole genome sequencing of subjects with Flagellar Growth Defects (FGD)'' financed by for the program Séquençage à haut débit 2012 to P.F.R.and the European Research Council (ERC) ACCENT Starting Grant 715289 to P.G.

800 # Figure legends

801 **Figure 1: Identification of two *CCDC146* gene variants in MMAF patients**

802 (A) Position of the observed variants in both probands. Electropherograms indicating the homozygous
803 state of the identified variant: variant c.1084C>T is a nonsense mutation, and c. c.2112Del is a single-
804 nucleotide deletion predicted to induce a translational frameshift. (B) Structure of the canonical
805 *CCDC146* gene transcript showing the position of the variants and their impact on translation. Variants
806 are annotated according to HGVS recommendations.

807 **Figure 2: *Ccdc146* KO mice are infertile and KO sperm exhibit a typical "multiple morphological**
808 **abnormalities of the flagellum (MMAF)" phenotype.**

809 (A) Number of pups produced by wild-type (+/+, WT), *CCDC146* heterozygote (+/-) and *CCDC146* knock-
810 out (-/-, KO) males (3 males per genotype) after mating with fertile WT females (2 females per male)
811 over a period of three months. (B) Sperm concentration and (C) sperm mobility. (D) Comparison of
812 testis weights (mg). (E) Illustration of WT and KO sperm morphologies stained with Papanicolaou and
813 observed under optic microscopy. Statistical comparisons were based on ordinary one-way ANOVA
814 tests (**** $p<0.0001$; *** $p<0.001$, **$p<0.01$, *$p<0.05$). Scale bar of images represents 10 µm.
815

816 **Figure 3: Histological evidence that spermiogenesis is disrupted in *Ccdc146* KO males and leads to a**
817 **strong decrease in sperm concentration in the epididymis.**
818 (A) Transversal sections of WT and KO testis stained with hematoxylin and eosin. The upper images
819 show the sections at low magnification (Scale bars: 50 µm) and the lower images are an enlargement
820 of the dotted square (scale bars: 10 µm). In the KO, spermatid nuclei were very elongated and no
821 flagella were visible within the seminiferous tubule lumen. (B) Transversal sections of WT and KO
822 epididymis stained with hematoxylin and eosin. Despite similar epididymis section diameters in WT
823 and KO testes, KO lumen were filled with round cells and contained few spermatozoa with abnormally-
824 shaped heads and flagella. The upper images show the sections at low magnification (scale bars 50 µm)
825 and the lower images are an enlargement of the dotted square (scale bars 10 µm).

826 **Figure 4: CCDC146 has a centriolar and pericentriolar localization in interphase somatic HEK-293T**
827 **cells.**

828 HEK-293T cells were immunolabeled for β-tubulin (green), centrin (yellow) and CCDC146 (magenta).
829 DNA was stained with Hoechst (blue). (A) CCDC146 localized to centrioles and/ or to the pericentriolar
830 material in interphase cells. The centrosomes of two cells are shown enlarged in A1 and A2. (B) In

831 serum starved cells with primary cilia, CCDC146 localizes to the basal body of primary cilia. The basal
832 body of two cells are shown enlarged in B1 and B2. CCDC146 is also present as dotted signal resembling
833 the pattern for centriolar satellite proteins. Scale bars on zoomed images: 2 µm.

834 **Figure 5: CCDC146 is a microtubule-associated protein (MAP) associating with microtubule-based**
835 **structures throughout the cell cycle.**

836 HEK-293T cells were immunolabeled with anti-β-tubulin (green), anti-centrin (yellow), and anti-
837 CCDC146 (magenta) Abs. DNA was stained with Hoechst (blue). In synchronized HEK-293T cells,
838 CCDC146 is observed associated with (A) mother centrioles and their corresponding procentrioles
839 during centriole duplication. (B) In non-synchronized cells, CCDC146 is observed associated with
840 microtubule tips during metaphase, (C) the central spindle during (C) anaphase and (D) telophase, and
841 (E) the midbody during cytokinesis. Images on the right show the enlargement of the dotted square in
842 the left image. Scale bar of zoomed images 2 µm.

843 **Figure 6: CCDC146 is expressed in late spermatocyte and in spermatids; CCDC146 protein is present**
844 **in spermatids and in epididymal spermatozoa in mouse.**

845 (A) mRNA expression levels of *Ccdc146* relative to *Actb* and *Hprt* in CCDC146-HA mouse pups' testes.
846 Extremely low expression was detected at day 9, corresponding to testes containing spermatogonia
847 and Sertoli cells only. *Ccdc146* expression was observed from postnatal day 18 (formation of secondary
848 spermatocytes), peaked at day 26 (formation of elongated spermatids), and subsequently decreased
849 from day 35 (formation of spermatozoa), suggesting that *Ccdc146* is particularly expressed in
850 elongated spermatids during spermatogenesis. (B) Western blot of HA-tagged and WT sperm showing
851 the specific band (arrow) corresponding to HA-tagged CCDC146 (CCDC146-HA) in epididymal whole
852 sperm. (C) Western blot of HA-tagged testis extracts at different postnatal days. The presence of HA-
853 tagged CCDC146 was revealed by an anti-HA Ab. Faint bands at the expected molecular weight are
854 observed at D26, D35 and in epididymal sperm.

855 **Figure 7: CCDC146 localizes to the flagellum but not to the centrioles of ejaculated human**
856 **spermatozoa.**

857 (A) Human ejaculated sperm were immunolabeled with Abs recognizing centrin (yellow), CCDC146
858 (magenta), and β-tubulin (green). DNA was stained with Hoechst (blue). (A1-A3) enlargement of dotted
859 square focused on sperm neck: no colocalization between CCDC146 and centrin. (A4) A faint signal for
860 CCDC146 is present along the length of the sperm flagellum. Scale bar of zoomed images: 1 µm. (B)
861 Human ejaculated sperm observed by expansion microscopy. Sperm were immunolabeled with anti-
862 CCDC146 (magenta) and anti-β-tubulin (green), and DNA was stained with Hoechst (blue). B1 and B5

863 show strong staining for CCDC146 in the axoneme, B3 showing the localization of the axoneme through
864 tubulin staining. B2, B4 and B6 show enlargements of the dotted square focused on the sperm neck.
865 CCDC146 did not colocalize with the centrioles at the base of the axoneme. The CCDC146 staining
866 observed probably corresponds to non-specific labeling of mitochondria.

867 **Figure 8: CCDC146 localizes to the flagellum of mouse epididymal spermatozoa.**

868 (A) Mouse epididymal spermatozoa observed with conventional IF. CCDC146-HA sperm were labeled
869 with anti-HA #1 (red) and anti-β-tubulin (green) Abs. DNA was stained with Hoechst (blue). The upper
870 image shows the sperm with merged immunostaining, and the lower images, the staining (red, green,
871 and merge) observed in the principal piece of the flagellum (Scale bars 10 µm). (B) Mouse epididymal
872 spermatozoa observed with expansion microscopy. CCDC146-HA sperm were immunolabeled with
873 anti-HA #2 (red) and anti-β-tubulin (green) Abs. DNA was stained with Hoechst (blue). The upper image
874 shows the sperm with merged immunostaining. The lower images show the staining (red, green, and
875 merge) observed in the principal piece of the flagellum. Strong punctiform signals were observed at
876 the level of axonemal breakages induced by the expansion process. White arrows indicate the zones
877 of the micro breaks (Scale bars correspond to 10 µm). (C) Similar experiment performed with a third
878 anti-HA Ab (#3). Scale bars 10 µm. (D) Western blot of whole sperm and flagella fraction extracts. The
879 presence of CCDC146-HA was revealed by an anti-HA Ab.

880 **Figure 9: CCDC146 localizes to the microtubule doublets of the axoneme in human and mouse**

881 (A) Sperm was double-stained with anti-tubulin Ab (green) and anti-CCDC146-Ab (magenta) and
882 observed by expansion microscopy. (B) The position of the CCDC146 signal with respect to the tubulin
883 signal was measured along the entire flagellum. CCDC146 signals were localized to different
884 compartments of the axoneme by the following method: the green signal is quite characteristic with
885 two peaks corresponding to the left and right microtubule doublet, it identifies five axonemal
886 compartments (left outer, left doublet, central pair, right doublet, and right outer). For each CCDC146
887 signal (magenta dots), the flagellum was perpendicularly cut (example, white bar in A) and the tubulin
888 and CCDC146 signals measured to assign each CCDC146 signal to a localization area. (C) Example of a
889 measurement obtained at the right bar shown in (A). (D) Histogram showing the distribution of
890 CCDC146 labeling in ejaculated human sperm 1, presented in (A). (E) Ejaculated human sperm double-
891 stained with anti-tubulin Ab (green) and anti-CCDC146-Ab (magenta). (F) Histogram showing how
892 CCDC146 labeling distributed in ejaculated human sperm 2. (G) Flagellum of a mouse epididymal
893 spermatozoa observed with expansion microscopy. CCDC146-HA sperm were immunolabeled with
894 anti-HA #2 (red) and anti-β-tubulin (green). The upper image shows the sperm with merged

895 immunostaining, and the lower images, the staining (red, green, and merge) observed in the principal
896 piece of the flagellum. Scale bars 10 µm.

897 **Figure 10: CCDC146 could be a microtubule inner protein in sperm: evidence from sarkosyl treatment**

898 (A) Western blot of WT and CCDC146-HA sperm extract solubilized with N-lauroylsarcosine (sarkosyl),
899 an anionic detergent. Sarkosyl was used at increasing concentrations (0.2, and 0.4%). The presence of
900 CCDC146-HA was detected by an anti-HA Ab. (B) Western blot of WT and CCDC146-HA sperm extracts
901 solubilized with alternative detergents (RIPA, CHAPS, Tris-HCl) and whole sperm extract solubilized in
902 Laemmli. The presence of CCDC146-HA was revealed by an anti-HA Ab. (C) Epididymal CCDC146-HA
903 sperm (C1-C2) and WT sperm (C3-C4), treated with sarkosyl (5 min, 0.2% sarkosyl) or not (NT), were
904 immunostained to reveal the HA-tag (red) and counterstained with Hoechst (blue). (C1) Without
905 treatment, a faint CCDC146 signal (white arrow heads) is observed along the flagellum from CCDC146-
906 HA sperm. (C2) Treatment with sarkosyl enhanced the CCDC146-HA signal along the sperm flagellum.
907 (C3) HA signal in WT non-treated (NT) sperm is present in the midpiece only, suggesting that this signal
908 is not specific. (C4) The HA signal in WT sperm is not enhanced by sarkosyl treatment. Scale bars 10 µm.

909 **Figure 11: The absence of CCDC146 causes defects of the head-tail coupling apparatus in epididymal**
910 **spermatozoa and duplication and mislocalization of centriole in testicular sperm.**

911 (A) Scanning electron microscopy of WT and *Ccdc146* KO epididymal spermatozoa showed aberrant
912 head morphologies and irregular head-tail coupling apparatus (HTCA) linking the sperm head with the
913 flagellum. (B) Testicular spermatozoa from WT (B1) and *Ccdc146* KO (B2-B6) mice immunolabeled with
914 anti-β-tubulin (magenta) and anti-centrin (B1-B3) or anti-γ-tubulin (B4-B6) (green) Abs. Centrioles
915 appeared to be normal (B2) in some spermatozoa, separated but partially attached to the head (B3,
916 B4), completely detached from the sperm head (B5) or duplicated (B6).

917 **Figure 12: Absence of elongation of axonemal microtubules at the base of the distal centriole.**

918 (A) In WT spermatids, the proximal centriole (PC) is linked to the base of the compacting nucleus (Nu)
919 through the basal plate (BP) and the capitulum (Ca), and the distal centriole (DC) is embedded in the
920 segmented column (SC). All these sperm-specific cytoskeletal structures make up the HTCA. At the
921 base of the distal centriole, axonemal microtubules (MT) grow. In *Ccdc146* KO elongating spermatids,
922 the overall structure of the HTCA is conserved, with the presence of the centrioles and the accessory
923 cytoskeletal structures. However, no axonemal microtubules are visible. (B) The adjunct (Ad) of the
924 proximal centriole is also preserved in *Ccdc146* KO spermatids. (C) Serial sections of the HTCA of a
925 *Ccdc146* KO spermatid confirm the absence of axonemal microtubules at the base of the distal
926 centriole during spermatid elongation. Scale bars 1 µm.

927 **Figure 13: Analysis of stages of spermatogenesis by IF reveals acrosome formation and manchette**
928 **elongation defects.**

929 Cross sections of WT and *Ccdc146* KO testes showing different stages of mouse spermatogenesis (I,
930 VII-XII). Stages were determined by double immunostaining for β-tubulin (red) and DPY19l2 (green;
931 acrosome localization), and DNA was stained with Hoechst (blue). (A) Very few mature spermatozoa
932 lined the lumen at stage VII-VIII in the KO. Cell orientations appear random from stage IX-X in the KO
933 and the tubules contain more advanced spermatid stages. The acrosome of elongating KO spermatids
934 had become abnormal by stage XII, and the manchette of elongated spermatids at stage I was longer
935 in the KO compared with the WT. (B) Typical spermatids from stages I-XII, showing details of acrosome
936 formation and manchette elongation. Scale bars stages VII-VIII 20 µm, scale bars IX-X, XII and I 10 µm.

937 **Figure 14: TEM of elongating spermatids from *Ccdc146* KO male shows ultrastructural defects of the**
938 **manchette.**

939 (A, B) Ultrastructural analysis of the manchette in WT elongating spermatids shows the normal thin
940 perinuclear ring, anchored below the acrosome and allowing a narrow array of microtubules to anchor.
941 (C-F) In elongating spermatids from *CCDC146* KO animals, the perinuclear ring was abnormally broad,
942 usually located on one side of the spermatid (red arrows), creating an asymmetric and wide bundle of
943 microtubules. The resulting manchette was wider and often longer than in WT animals. (E, F) The
944 tubulin nucleation location was sometimes ectopic in the KO and coincided with irregularly shaped
945 sperm heads.

946 **Figure 15: The axonemes of *Ccdc146* KO spermatids present multiple defects visible under TEM.**

947 (A1) A longitudinal section of a WT flagellum shows a typical structure of the principal piece, with outer
948 dense fibers (ODF) at the periphery, microtubules (MT) in the center, and mitochondria (Mi) aligned
949 along the flagellum. (B1) A longitudinal section of a *Ccdc146* KO flagellum shows a disorganized
950 midpiece, with altered mitochondria, the presence of an amorphous fibrous sheath (FS) and altered
951 microtubules. (B) Longitudinal section of a *Ccdc146* KO sperm showing dispersed and non-assembled
952 flagellar material in a cytoplasmic mass. The right-hand image is the enlargement of the red square,
953 showing the presence of an external ring of mitochondria surrounding an outer dense fiber ring devoid
954 of microtubular material. (C) Longitudinal section of another *Ccdc146* KO sperm showing a similar
955 abnormal midpiece structure. The right-hand image is the enlargement of the red square, showing the
956 presence of an external ring of mitochondria surrounding an outer dense fiber ring devoid of
957 microtubular material.

958

959 **Appendix – Figure 1. Relative mRNA expression levels for human and mouse CCDC146 transcripts.**

960 (A) CCDC146 mRNA levels measured in different tissues/cells in humans using Affymetrix microarrays
961 (data available from the Genevestigator database, https://genevestigator.com). Red rectangles
962 highlight the high expression level in male reproductive organs. (B) Similar data for mice. Data were
963 generated with Genevestigator (Hruz T, Laule O, Szabo G, Wessendorp F, Bleuler S, Oertle L, Widmayer
964 P, Gruissem W and P Zimmermann (2008) Genevestigator V3: a reference expression database for the
965 meta-analysis of transcriptomes. Advances in Bioinformatics 2008, 420747)

966 **Appendix – Figure 2. Molecular strategy used to generate *Ccdc146* KO mice by CRISPR/Cas9**

967 The exonic structure of mouse *Ccdc146* is shown and the coding sequence indicated in black. Exon 2,
968 the first coding sequence, was targeted by an RNA guide (5'-CCT ACA GTT AAC ATT CGG G-3) and the
969 Cas9 induced a deletion of four nucleotides upstream the PAM sequence, as indicated by the red box.
970 Electropherogram presenting the WT and the homozygote deletion are shown.

971 **Appendix – Figure 3. Increased levels of apoptosis in testes from *Ccdc146* KO mice.** The TUNEL assay
972 was used to visualize double-strand DNA breaks, as an indication of the level of apoptosis during WT
973 and KO spermatogenesis. (A) Comparison of the % of tubules per testis cross-section containing at least
974 one TUNEL-positive cell in WT, heterozygote, and *Ccdc146* KO animals. Number of sections counted
975 per genotype n=13-20, 3 different mice per genotype. (B) The majority of TUNEL-positive cells in the
976 WT corresponded to pachytene cells undergoing meiosis (B, WT zoomed image) whereas the
977 localization of TUNEL-positive cells in KO was more scattered. (C) Control testis section treated with
978 H_20_2. Statistical comparisons according to ordinary one-way ANOVA test (**** $p<0.0001$; *** $p<0.001$,
979 ** $p<0.01$, * $p<0.05$). Scale bar of zoomed images 50 µm.

980 **Appendix – Figure 4. CCDC146 does not colocalize with the centriolar satellite marker PCM1.**

981 (A) HEK-293T cells were double immunolabeled for PCM1 (cyan) and CCDC146 (magenta). (A1-A4)
982 Images on the right show the enlargement of the dotted squares in the left image. PCM1 surrounds
983 the CCDC146 signal, but no colocalization is observed, suggesting that CCDC146 is not a centriolar
984 satellite protein. DNA was stained with Hoechst (blue). Scale bars on zoomed images represent 2 µm.

985 **Appendix – Figure 5. CCDC146 shows a similar localization to the centrosome and to the midbody in**
986 **primary HFF cells.** (A) Primary human foreskin fibroblast (HFF) cells were triple immunolabeled with
987 anti-β-tubulin (green), anti-centrin (yellow, showing the centrioles) and anti-CCDC146 (magenta). (A1)
988 The right-hand images show the enlargement of the dotted squares in the left-hand image. CCDC146

989 localized to and around the centrioles. (B) similar staining showing co-labeling of the midbody during
990 cytokinesis by anti-CCDC146 Abs (B2). Scale bar of zoomed images 2 µm.

991 **Appendix – Figure 6. Molecular strategy used to generate *HA-tagged CCDC146* mice by CRISPR/Cas9**

992 The reference CCDC146 mouse transcript is ENSMUST00000115245.7 (GRCm38.p6). Exon 2, the first
993 coding sequence, was targeted by an RNA guide (5'- TAC TTT AGA ACT GTG AAA AAT GG -3'). We used
994 a single-stranded DNA (ssDNA) template to insert the HA sequence (5'-TAC CCA TAC GAT GTT CCA GAT
995 TAC GCT-3') upstream of the PAM sequence.

996 **Appendix – Figure 7. Centrioles are identified by anti-POC5 Abs in expanded human ejaculated**
997 **spermatozoa.** Human control sperm were co-stained, after expansion, with anti- α+β-tubulin (green)
998 and anti-POC5 (magenta) Abs. The centrosomal protein POC5 locates to centrioles at the base of the
999 axoneme. Scale bars 5 µm.

1000 **Appendix – Figure 8. Non-specific midpiece staining in mouse sperm by rabbit secondary antibody.**

1001 Mouse sperm were stained with secondary antibodies only. Scale bars 10 µm.

1002 **Appendix – Figure 9. Sperm sarkosyl treatment corroborates the presence of CCDC146 along the**
1003 **mouse flagellum.**

1004 CCDC146-HA sperm (A1-A2) and epididymal WT (A3-A4) not treated or treated (5 min, 0.2% sarkosyl),
1005 were immunostained with anti-HA Ab (red) and counterstained with Hoechst (blue). (A1) Without
1006 treatment, a faint CCDC146-HA signal was observed along the CCDC146-HA principal piece. The strong
1007 staining in the midpiece is not specific (see panel B) (A2) After treatment with sarkosyl, the CCDC146-
1008 HA signal along the sperm principal piece was enhanced (white arrows), whereas the signal in the
1009 midpiece decreased. (A3) WT untreated (NT) sperm exhibited almost no CCDC146-HA signal in the
1010 principal piece. The midpiece is however strongly stained (not specific see panel B) (A4) The HA signal
1011 is not enhanced in WT principal piece by sarkosyl treatment, suggesting that the enhanced signal
1012 observed with sarkosyl on CCDC146-HA sperm is specific. (B) CCDC146-HA sperm were immunolabeled
1013 with secondary antibody only. Strong staining is observed on the midpiece, confirming its non-specific
1014 nature. Scale bars 10 µm.

1015 **Appendix – Figure 10. Lack of CCDC146 causes centriole duplication and mislocalization in *Ccdc146***
1016 **KO spermatids.**

1017 Ultrastructural analysis of centrioles in adult mouse WT (A, B) and *Ccdc146* KO (C-H) testis sections.

1018 (A) In WT spermatids, the proximal centriole is linked to the base of the compacting nucleus through
1019 the basal plate and the capitulum, and the distal centriole is embedded in the segmented column.
1020 These sperm-specific cytoskeletal structures make up the head-to-tail coupling apparatus (HTCA). (B)
1021 In WT elongated spermatids, the different components of the axonemal structures (microtubules and
1022 ODF) were visible downstream the distal centriole. (C) In *Ccdc146* KO elongating spermatids, the
1023 overall structure of the HTCA was conserved, with the presence of the centrioles and the accessory
1024 cytoskeletal structures. However, the HTCAs were often duplicated (C, E, F) and separated from their
1025 usual nuclear attachment site (C-F, H), and sometimes misplaced far away from the nucleus (F), likely
1026 preventing axoneme elongation. (F) The arrow indicates the misplaced centrioles at the end of the
1027 manchette. (G, H) In elongated spermatids with condensed nucleus, malformed and detached
1028 centrioles with poorly-assembled or missing flagella compared to the WT (B) can be seen.

1029 **Appendix –Figure 11. Spermatid head shape is aberrant in the absence of CCDC146.** Comparative
1030 ultrastructural analysis of the spermatid head in WT (A-D) and *Ccdc146* KO (E-H) testis sections.

1031 (A, E) Spermatid nuclei at the beginning of elongation. KO spermatid nuclei showing nuclear membrane
1032 invaginations and irregular shape that were not present in the WT. The acrosome in the KO sperm
1033 appeared intact. (B, F) Spermatid nuclei in elongating spermatids. Whereas nucleus elongation is
1034 symmetric in the WT, in the *CCDC146*-KO, more pronounced head invaginations are observed. (C, G)
1035 Elongated spermatids. Although nuclear condensation appeared normal in both WT and KO nuclei,
1036 vacuolization is observed in KO nucleus. (D, H) Elongated KO spermatids showed malformed elongated
1037 nuclear shapes with frequent invaginations and poorly-assembled flagella (H) compared to the WT (D).

1038

1039

1040 ## References

1041 1. Boivin, J., et al., *International estimates of infertility prevalence and treatment-seeking:*
1042 *potential need and demand for infertility medical care.* Hum.Reprod., 2007. **22**(6): p. 1506-
1043 1512.
1044 2. Uhlén, M., et al., *Transcriptomics resources of human tissues and organs.* Mol Syst Biol, 2016.
1045 **12**(4): p. 862.
1046 3. Houston, B.J., et al., *A systematic review of the validated monogenic causes of human male*
1047 *infertility: 2020 update and a discussion of emerging gene-disease relationships.* Hum Reprod
1048 Update, 2021. **28**(1): p. 15-29.
1049 4. Beurois, J., et al., *Genetics of teratozoospermia: Back to the head.* Best Pract Res Clin
1050 Endocrinol Metab, 2020. **34**(6): p. 101473.
1051 5. Touré, A., et al., *The genetic architecture of morphological abnormalities of the sperm tail.* Hum
1052 Genet, 2021. **140**(1): p. 21-42.
1053 6. Wang, J., et al., *Clinical detection, diagnosis and treatment of morphological abnormalities of*
1054 *sperm flagella: A review of literature.* Front Genet, 2022. **13**: p. 1034951.
1055 7. Sironen, A., et al., *Sperm defects in primary ciliary dyskinesia and related causes of male*
1056 *infertility.* Cell Mol Life Sci, 2020. **77**(11): p. 2029-2048.
1057 8. Lores, P., et al., *Homozygous missense mutation L673P in adenylate kinase 7 (AK7) leads to*
1058 *primary male infertility and multiple morphological anomalies of the flagella but not to primary*
1059 *ciliary dyskinesia.* Hum Mol Genet, 2018.
1060 9. Coutton, C., et al., *Bi-allelic Mutations in ARMC2 Lead to Severe Astheno-Teratozoospermia*
1061 *Due to Sperm Flagellum Malformations in Humans and Mice.* Am J Hum Genet, 2019. **104**(2):
1062 p. 331-340.
1063 10. Shen, Q., et al., *Bi-allelic truncating variants in CFAP206 cause male infertility in human and*
1064 *mouse.* Hum Genet, 2021. **140**(9): p. 1367-1377.
1065 11. Cong, J., et al., *Homozygous mutations in CCDC34 cause male infertility with*
1066 *oligoasthenoteratozoospermia in humans and mice.* J Med Genet, 2022. **59**(7): p. 710-718.
1067 12. Kherraf, Z.E., et al., *A Homozygous Ancestral SVA-Insertion-Mediated Deletion in WDR66*
1068 *Induces Multiple Morphological Abnormalities of the Sperm Flagellum and Male Infertility.* Am
1069 J Hum Genet, 2018. **103**(3): p. 400-412.
1070 13. Coutton, C., et al., *Mutations in CFAP43 and CFAP44 cause male infertility and flagellum defects*
1071 *in Trypanosoma and human.* Nat Commun, 2018. **9**(1): p. 686.
1072 14. Liu, C., et al., *Deleterious variants in X-linked CFAP47 induce asthenoteratozoospermia and*
1073 *primary male infertility.* Am J Hum Genet, 2021. **108**(2): p. 309-323.
1074 15. Liu, S., et al., *CFAP61 is required for sperm flagellum formation and male fertility in human and*
1075 *mouse.* Development, 2021. **148**(23).
1076 16. Li, W., et al., *Biallelic mutations in CFAP65 cause male infertility with multiple morphological*
1077 *abnormalities of the sperm flagella in humans and mice.* J Med Genet, 2020. **57**(2): p. 89-95.
1078 17. Dong, F.N., et al., *Absence of CFAP69 Causes Male Infertility due to Multiple Morphological*
1079 *Abnormalities of the Flagella in Human and Mouse.* Am J Hum Genet, 2018. **102**(4): p. 636-648.
1080 18. Beurois, J., et al., *CFAP70 mutations lead to male infertility due to severe astheno-*
1081 *teratozoospermia. A case report.* Hum Reprod, 2019. **34**(10): p. 2071-2079.
1082 19. Martinez, G., et al., *Biallelic variants in MAATS1 encoding CFAP91, a calmodulin-associated and*
1083 *spoke-associated complex protein, cause severe astheno-teratozoospermia and male*
1084 *infertility.* J Med Genet, 2020. **57**(10): p. 708-716.
1085 20. Ben Khelifa, M., et al., *Mutations in DNAH1, which encodes an inner arm heavy chain dynein,*
1086 *lead to male infertility from multiple morphological abnormalities of the sperm flagella.*
1087 American Journal of Human Genetics, 2014. **94**(1): p. 95-104.
1088 21. Liu, C., et al., *Bi-allelic DNAH8 Variants Lead to Multiple Morphological Abnormalities of the*
1089 *Sperm Flagella and Primary Male Infertility.* Am J Hum Genet, 2020. **107**(2): p. 330-341.

1090 22. Martinez, G., et al., *Whole-exome sequencing identifies mutations in FSIP2 as a recurrent cause*
1091 *of multiple morphological abnormalities of the sperm flagella.* Hum Reprod, 2018. **33**(10): p.
1092 1973-1984.
1093 23. Lorès, P., et al., *A missense mutation in IFT74, encoding for an essential component for*
1094 *intraflagellar transport of Tubulin, causes asthenozoospermia and male infertility without*
1095 *clinical signs of Bardet-Biedl syndrome.* Hum Genet, 2021. **140**(7): p. 1031-1043.
1096 24. Kherraf, Z.E., et al., *Whole exome sequencing of men with multiple morphological*
1097 *abnormalities of the sperm flagella reveals novel homozygous QRICH2 mutations.* Clin Genet,
1098 2019. **96**(5): p. 394-401.
1099 25. Liu, C., et al., *Homozygous mutations in SPEF2 induce multiple morphological abnormalities of*
1100 *the sperm flagella and male infertility.* J Med Genet, 2020. **57**(1): p. 31-37.
1101 26. Liu, W., et al., *Bi-allelic Mutations in TTC21A Induce Asthenoteratospermia in Humans and*
1102 *Mice.* Am J Hum Genet, 2019. **104**(4): p. 738-748.
1103 27. Lorès, P., et al., *Mutations in TTC29, Encoding an Evolutionarily Conserved Axonemal Protein,*
1104 *Result in Asthenozoospermia and Male Infertility.* Am J Hum Genet, 2019. **105**(6): p. 1148-1167.
1105 28. Firat-Karalar, E.N., et al., *Proteomic analysis of mammalian sperm cells identifies new*
1106 *components of the centrosome.* J Cell Sci, 2014. **127**(Pt 19): p. 4128-4133.
1107 29. Almeida, F., et al., *The Human Centrosomal Protein CCDC146 Binds Chlamydia trachomatis*
1108 *Inclusion Membrane Protein CT288 and Is Recruited to the Periphery of the Chlamydia-*
1109 *Containing Vacuole.* Front Cell Infect Microbiol, 2018. **8**(article 254).
1110 30. Blanco-Ameijeiras, J., P. Lozano-Fernández, and E. Martí, *Centrosome maturation - in tune with*
1111 *the cell cycle.* J Cell Sci, 2022. **135**(2/jcs.259395).
1112 31. Wu, B., et al., *The coupling apparatus of the sperm head and tail†.* Biol Reprod, 2020. **102**(5):
1113 p. 988-998.
1114 32. Fishman, E.L., et al., *A novel atypical sperm centriole is functional during human fertilization.*
1115 Nat Commun, 2018. **9**(1): p. 2210.
1116 33. Manandhar, G., et al., *Centrosome reduction during mouse spermiogenesis.* Dev Biol, 1998.
1117 **203**(2): p. 424-434.
1118 34. Sha, Y.W., et al., *A homozygous CEP135 mutation is associated with multiple morphological*
1119 *abnormalities of the sperm flagella (MMAF).* Gene, 2017. **633**: p. 48-53.
1120 35. Zhang, X., et al., *CEP128 is involved in spermatogenesis in humans and mice.* Nat Commun,
1121 2022. **13**(1): p. 1395.
1122 36. Lv, M., et al., *Homozygous mutations in DZIP1 can induce asthenoteratospermia with severe*
1123 *MMAF.* J Med Genet, 2020. **57**(7): p. 445-453.
1124 37. Sha, Y., et al., *Biallelic mutations of CFAP58 are associated with multiple morphological*
1125 *abnormalities of the sperm flagella.* Clin Genet, 2021. **99**(3): p. 443-448.
1126 38. Zhu, Z.J., et al., *Novel mutation in ODF2 causes multiple morphological abnormalities of the*
1127 *sperm flagella in an infertile male.* Asian J Androl, 2022. **24**(5): p. 463-472.
1128 39. Nakagawa, Y., et al., *Outer dense fiber 2 is a widespread centrosome scaffold component*
1129 *preferentially associated with mother centrioles: its identification from isolated centrosomes.*
1130 Mol Biol Cell, 2001. **12**(6): p. 1687-1697.
1131 40. Hall, E.A., et al., *Acute versus chronic loss of mammalian Azi1/Cep131 results in distinct ciliary*
1132 *phenotypes.* PLoS Genet, 2013. **9**(12): p. e1003928.
1133 41. Pasek, R.C., et al., *Coiled-coil domain containing 42 (Ccdc42) is necessary for proper sperm*
1134 *development and male fertility in the mouse.* Dev Biol, 2016. **412**(2): p. 208-18.
1135 42. Kherraf, Z.E., et al., *Whole-exome sequencing improves the diagnosis and care of men with*
1136 *non-obstructive azoospermia.* Am J Hum Genet, 2022. **109**(3): p. 508-517.
1137 43. Odabasi, E., U. Batman, and E.N. Firat-Karalar, *Unraveling the mysteries of centriolar satellites:*
1138 *time to rewrite the textbooks about the centrosome/cilium complex.* Mol Biol Cell, 2020. **31**(9):
1139 p. 866-872.
1140 44. Zindy, F., et al., *Control of spermatogenesis in mice by the cyclin D-dependent kinase inhibitors*
1141 *p18(Ink4c) and p19(Ink4d).* Mol Cell Biol, 2001. **21**(9): p. 3244-55.

1142 45. Gambarotto, D., et al., *Imaging cellular ultrastructures using expansion microscopy (U-ExM).*
1143 Nat Methods, 2019. **16**(1): p. 71-74.
1144 46. Yanagisawa, H.A., et al., *FAP20 is an inner junction protein of doublet microtubules essential*
1145 *for both the planar asymmetrical waveform and stability of flagella in Chlamydomonas.* Mol
1146 Biol Cell, 2014. **25**(9): p. 1472-83.
1147 47. Witman, G.B., et al., *Chlamydomonas flagella. I. Isolation and electrophoretic analysis of*
1148 *microtubules, matrix, membranes, and mastigonemes.* J Cell Biol, 1972. **54**(3): p. 507-39.
1149 48. Linck, R.W., *Flagellar doublet microtubules: fractionation of minor components and alpha-*
1150 *tubulin from specific regions of the A-tubule.* J Cell Sci, 1976. **20**(2): p. 405-39.
1151 49. Kirima, J. and K. Oiwa, *Flagellar-associated Protein FAP85 Is a Microtubule Inner Protein That*
1152 *Stabilizes Microtubules.* Cell Struct Funct, 2018. **43**(1): p. 1-14.
1153 50. Simerly, C., et al., *Post-Testicular Sperm Maturation: Centriole Pairs, Found in Upper*
1154 *Epididymis, are Destroyed Prior to Sperm's Release at Ejaculation.* Sci Rep, 2016. **6**: p. 31816.
1155 51. Kierszenbaum, A.L., et al., *The acroplaxome is the docking site of Golgi-derived myosin*
1156 *Va/Rab27a/b- containing proacrosomal vesicles in wild-type and Hrb mutant mouse*
1157 *spermatids.* Biol.Reprod., 2004. **70**(5): p. 1400-1410.
1158 52. Martinez, G., et al., *Oligogenic heterozygous inheritance of sperm abnormalities in mouse.*
1159 Elife, 2022. **11**.
1160 53. Collins, S.A., W.T. Walker, and J.S. Lucas, *Genetic Testing in the Diagnosis of Primary Ciliary*
1161 *Dyskinesia: State-of-the-Art and Future Perspectives.* J Clin Med, 2014. **3**(2): p. 491-503.
1162 54. Shoemark, A., L. Ozerovitch, and R. Wilson, *Aetiology in adult patients with bronchiectasis.*
1163 Respir Med, 2007. **101**(6): p. 1163-70.
1164 55. Li, Z.Z., et al., *The novel testicular enrichment protein Cfap58 is required for Notch-associated*
1165 *ciliogenesis.* Biosci Rep, 2020. **40**(1).
1166 56. Cuveillier, C., et al., *Beyond Neuronal Microtubule Stabilization: MAP6 and CRMPS, Two*
1167 *Converging Stories.* Front Mol Neurosci, 2021. **14**: p. 665693.
1168 57. Ma, M., et al., *Structure of the Decorated Ciliary Doublet Microtubule.* Cell, 2019. **179**(4): p.
1169 909-922.e12.
1170 58. Jardin, I., et al., *SARAF and EFHB Modulate Store-Operated Ca(2+) Entry and Are Required for*
1171 *Cell Proliferation, Migration and Viability in Breast Cancer Cells.* Cancers (Basel), 2021. **13**(16).
1172 59. Segal, R.A., et al., *Mutant strains of Chlamydomonas reinhardtii that move backwards only.* J
1173 Cell Biol, 1984. **98**(6): p. 2026-34.
1174 60. Tam, L.W. and P.A. Lefebvre, *The Chlamydomonas MBO2 locus encodes a conserved coiled-coil*
1175 *protein important for flagellar waveform conversion.* Cell Motil Cytoskeleton, 2002. **51**(4): p.
1176 197-212.
1177 61. Shi, Z., et al., *Potential Novel Modules and Hub Genes as Prognostic Candidates of Thyroid*
1178 *Cancer by Weighted Gene Co-Expression Network Analysis.* Int J Gen Med, 2021. **14**: p. 9433-
1179 9444.
1180 62. Kasak, L., et al., *Bi-allelic Recessive Loss-of-Function Variants in FANCM Cause Non-obstructive*
1181 *Azoospermia.* Am J Hum Genet, 2018. **103**(2): p. 200-212.
1182 63. Amargant, F., et al., *The human sperm basal body is a complex centrosome important for*
1183 *embryo preimplantation development.* Mol Hum Reprod, 2021. **27**(11:gaab062).
1184 64. Lehti, M.S. and A. Sironen, *Formation and function of the manchette and flagellum during*
1185 *spermatogenesis.* Reproduction, 2016. **151**(4): p. R43-54.
1186 65. O'Donnell, L., et al., *An essential role for katanin p80 and microtubule severing in male gamete*
1187 *production.* PLoS Genet, 2012. **8**(5): p. e1002698.
1188 66. Ho, U.Y., et al., *WDR62 is required for centriole duplication in spermatogenesis and manchette*
1189 *removal in spermiogenesis.* Commun Biol, 2021. **4**(1): p. 645.
1190 67. Zhu, F., et al., *Biallelic SUN5 Mutations Cause Autosomal-Recessive Acephalic Spermatozoa*
1191 *Syndrome.* Am J Hum Genet, 2016. **99**(4): p. 942-949.
1192 68. Yuan, S., et al., *Spata6 is required for normal assembly of the sperm connecting piece and tight*
1193 *head-tail conjunction.* Proc.Natl.Acad.Sci.U.S.A, 2015. **112**(5): p. E430-E439.

1194 69. Hoyer-Fender, S., *Development of the Connecting Piece in ODF1-Deficient Mouse Spermatids.*
1195 Int J Mol Sci, 2022. **23**(18:10280).
1196 70. Dunleavy, J.E.M., et al., *Katanin-like 2 (KATNAL2) functions in multiple aspects of haploid male*
1197 *germ cell development in the mouse.* PLoS Genet, 2017. **13**(11): p. e1007078.
1198 71. Giordano, T., et al., *Loss of the deglutamylase CCP5 perturbs multiple steps of spermatogenesis*
1199 *and leads to male infertility.* J Cell Sci, 2019. **132**(3).
1200 72. Wang, Y., et al., *Variability in the morphologic assessment of human sperm: use of the strict*
1201 *criteria recommended by the World Health Organization in 2010.* Fertil Steril, 2014. **101**(4): p.
1202 945-9.
1203 73. Schindelin, J., et al., *Fiji: an open-source platform for biological-image analysis.* Nat Methods,
1204 2012. **9**(7): p. 676-82.
1205 74. Mazo, G., *QuickFigures: A toolkit and ImageJ PlugIn to quickly transform microscope images*
1206 *into scientific figures.* PLoS One, 2021. **16**(11): p. e0240280.
1207 75. Reynolds, E.S., *The use of lead citrate at high pH as an electron-opaque stain in electron*
1208 *microscopy.* J Cell Biol, 1963. **17**(1): p. 208-12.
1209 76. Pierre, V., et al., *Absence of Dpy19l2, a new inner nuclear membrane protein, causes*
1210 *globozoospermia in mice by preventing the anchoring of the acrosome to the nucleus.*
1211 Development, 2012. **139**(16): p. 2955-65.

1212

Figure 1

A

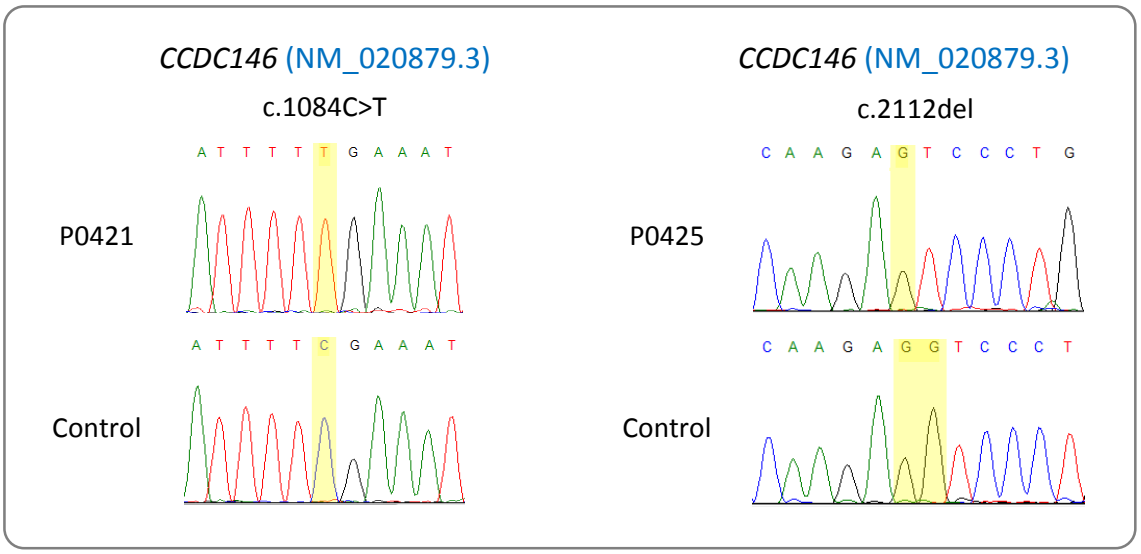
CCDC146 (NM_020879.3)
c.1084C>T
P0421
Control
CCDC146 (NM_020879.3)
c.2112del
P0425
Control

B

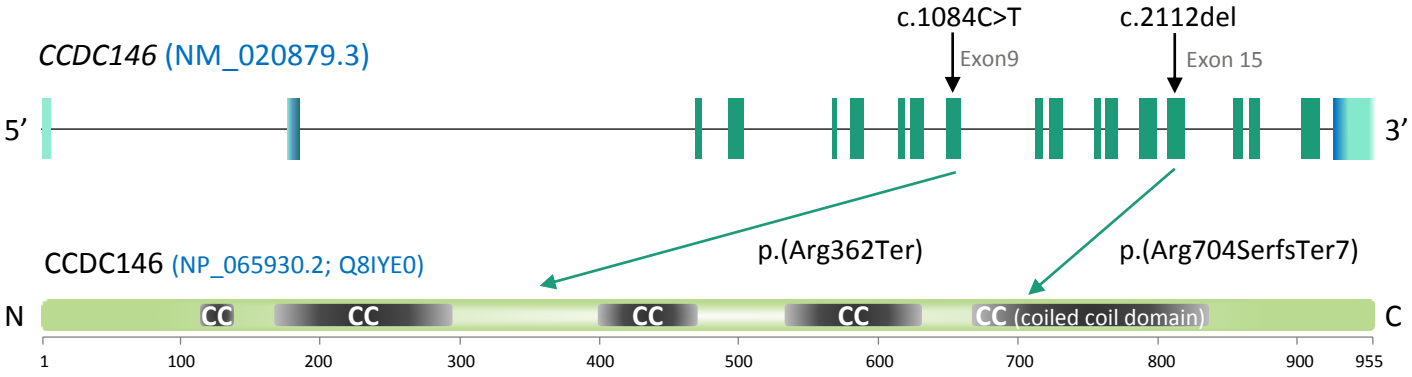
CCDC146 (NM_020879.3)
c.1084C>T
Exon9
c.2112del
Exon 15
5'
3'
CCDC146 (NP_065930.2; Q8IYE0)
p.(Arg362Ter)
p.(Arg704SerfsTer7)
N
CC
CC
CC
CC
CC (coiled coil domain)
C
1
100
200
300
400
500
600
700
800
900
955

Figure 2

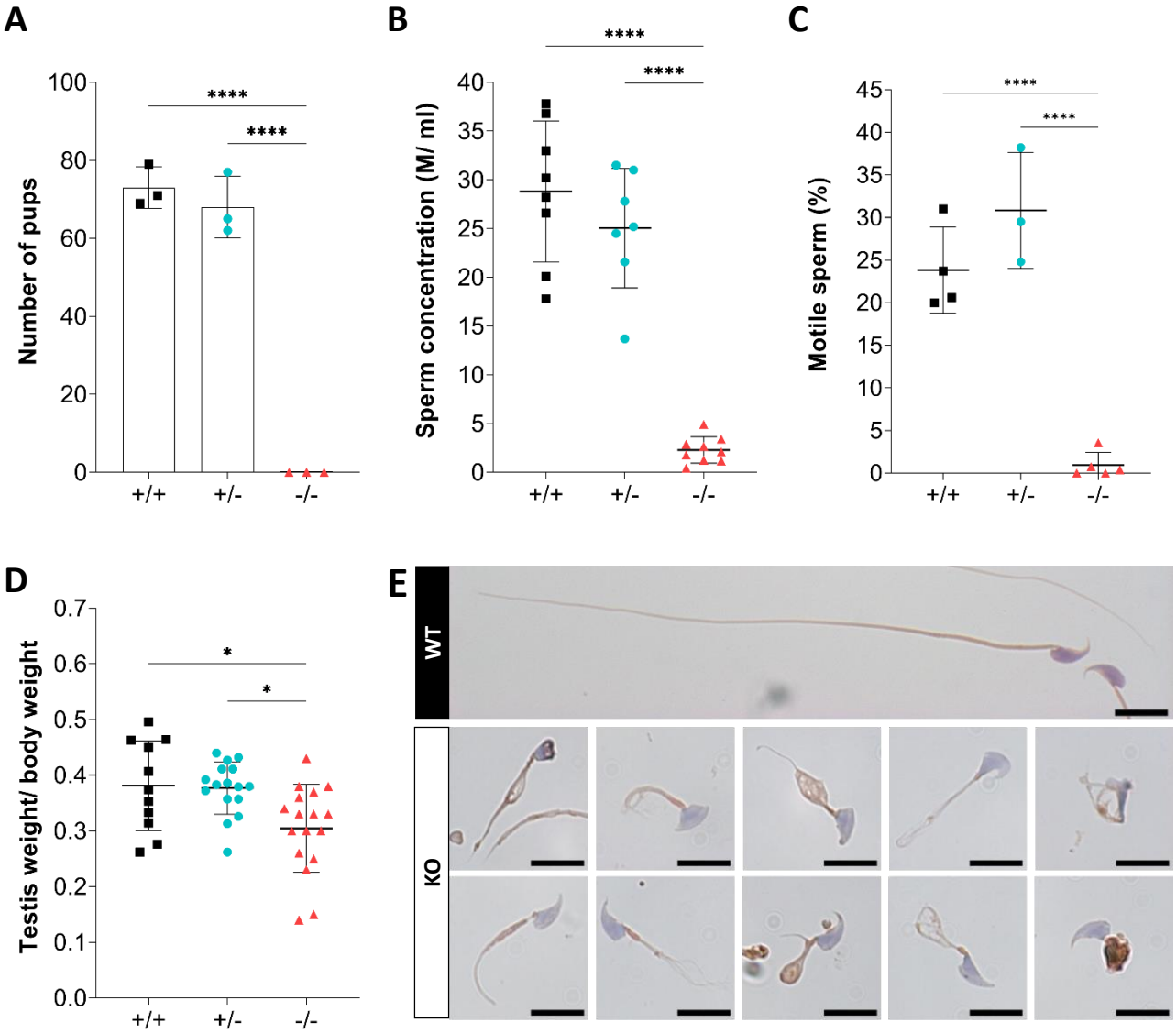
A
Number of pups
100
80
60
40
20
0
****
****
+/+
+/-
-/-
B
Sperm concentration (M/ ml)
40
35
30
25
20
15
10
5
0
****
****
+/+
+/-
-/-
C
Motile sperm (%)
45
40
35
30
25
20
15
10
5
0
****
****
+/+
+/-
-/-
D
Testis weight/ body weight
0.7
0.6
0.5
0.4
0.3
0.2
0.1
0.0
*
*
+/+
+/-
-/-
E
WT
KO

Figure 3

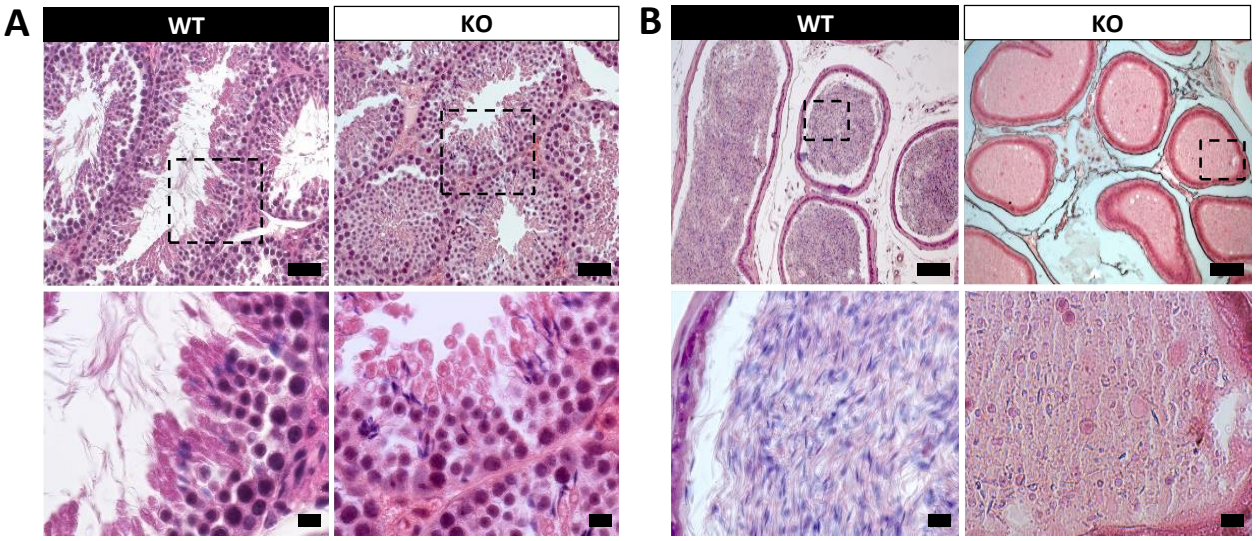

Figure 4

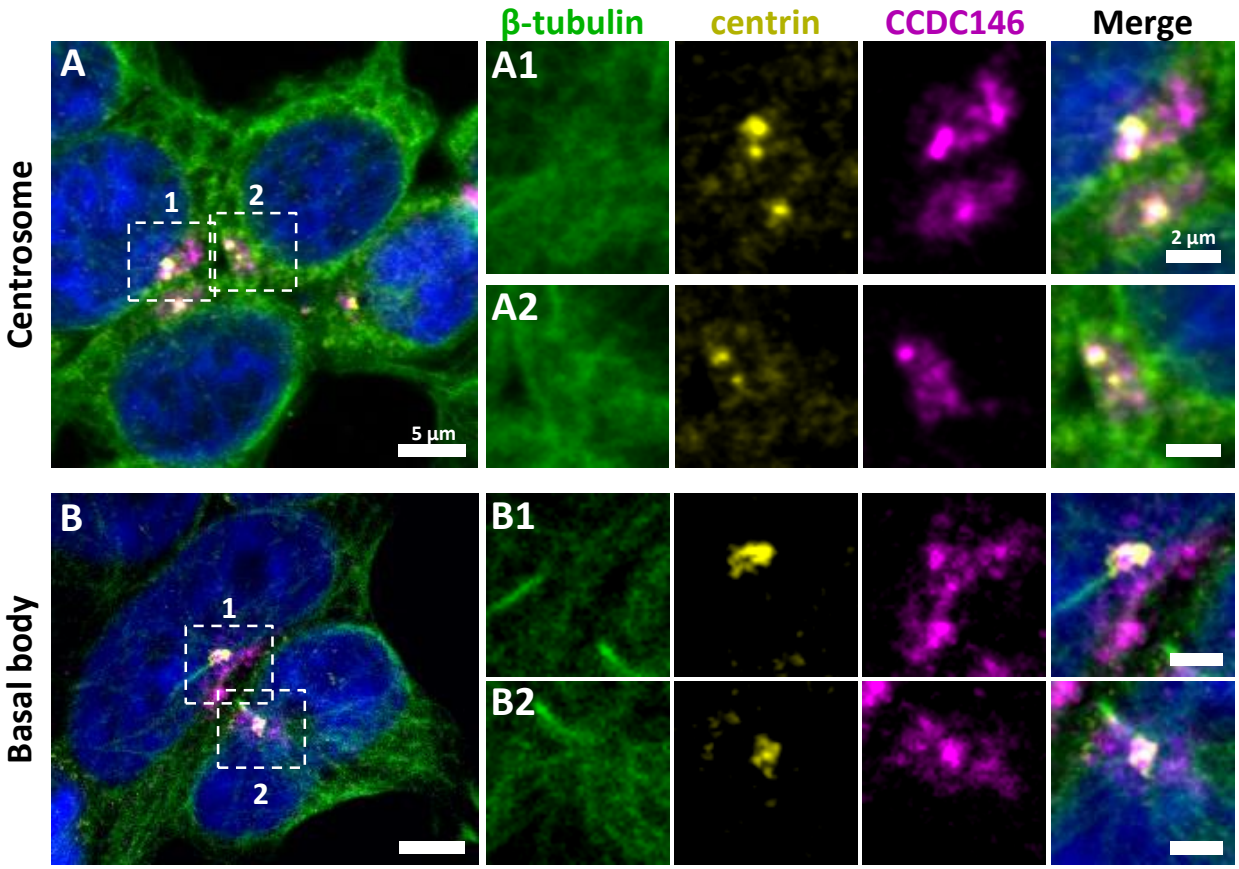
β-tubulin
centrin
CCDC146
Merge
Centrosome
Basal body
A
A1
A2
B
B1
B2
1
2
5 µm
2 µm

Figure 5

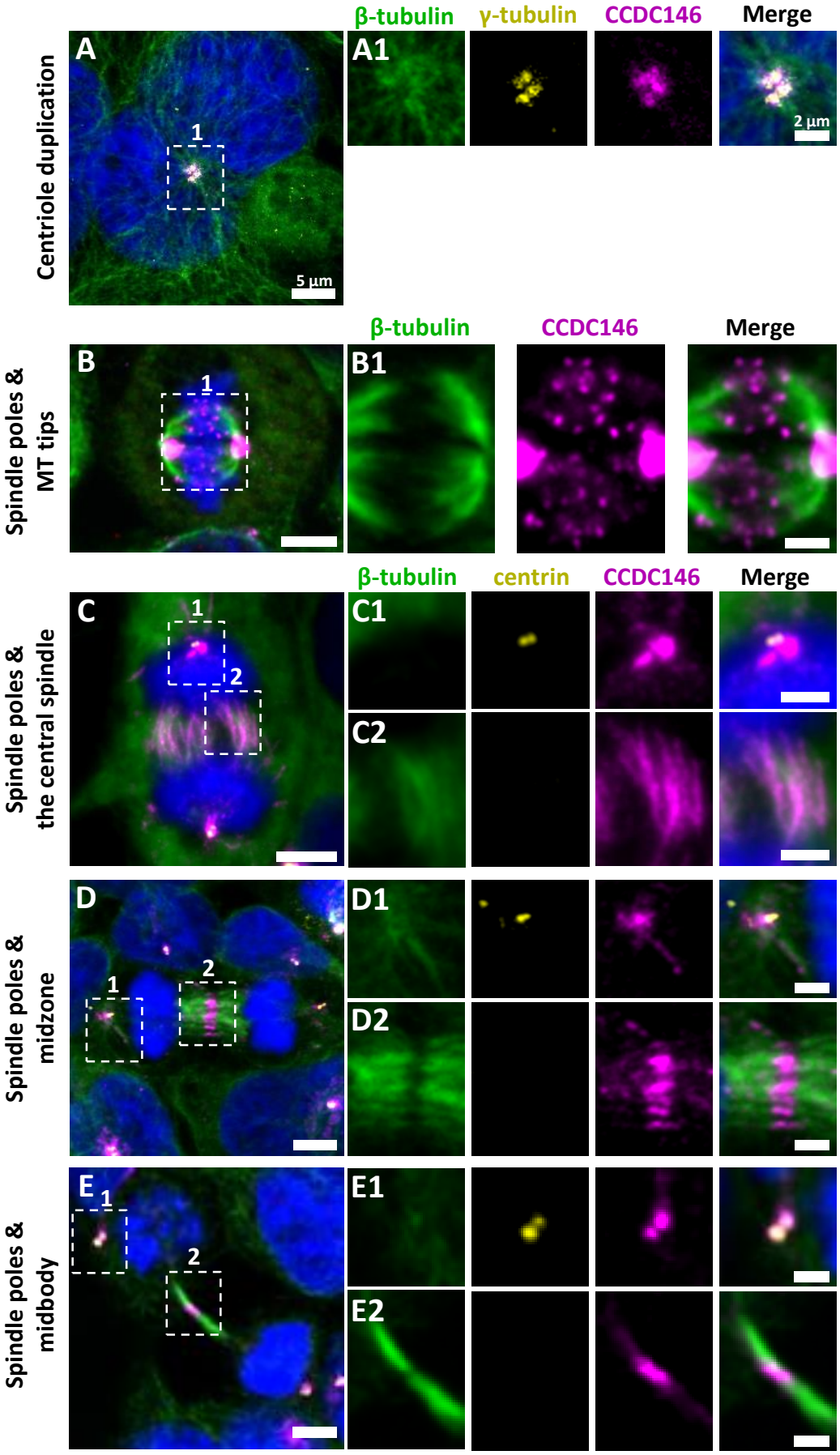
β-tubulin
γ-tubulin
CCDC146
Merge
Centriole duplication
A
A1
1
5 µm
2 µm
β-tubulin
CCDC146
Merge
Spindle poles & MT tips
B
B1
1
β-tubulin
centrin
CCDC146
Merge
Spindle poles & the central spindle
C
C1
C2
1
2
Spindle poles & midzone
D
D1
D2
1
2
Spindle poles & midbody
E
E1
E2
1
2

Figure 6

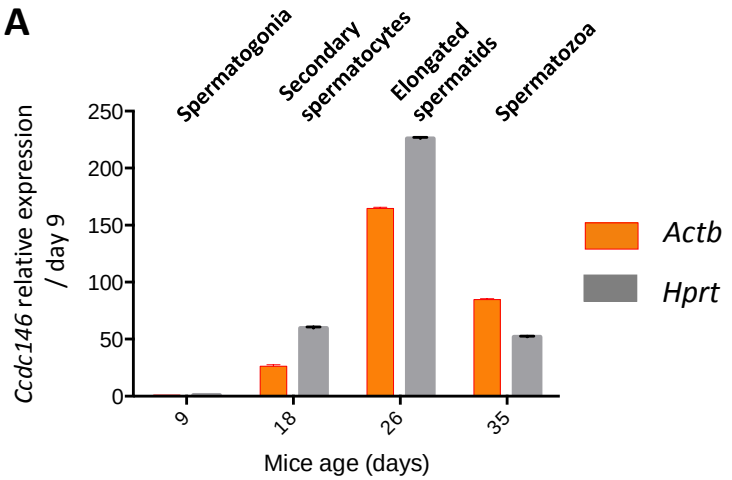
A
Spermatogonia
Secondary spermatocytes
Elongated spermatids
Spermatozoa
Ccdc146 relative expression / day 9
250
200
150
100
50
0
9
18
26
35
Mice age (days)
Actb
Hprt

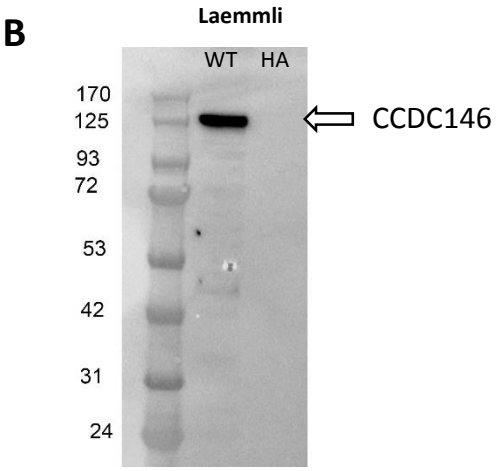
B
Laemmli
WT
HA
170
125
93
72
53
42
31
24
CCDC146

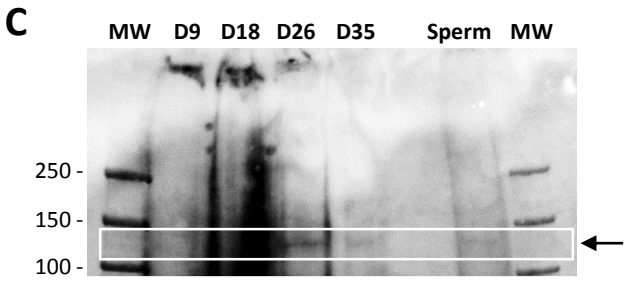
C
MW
D9
D18
D26
D35
Sperm
MW
250 -
150 -
100 -

Figure 7

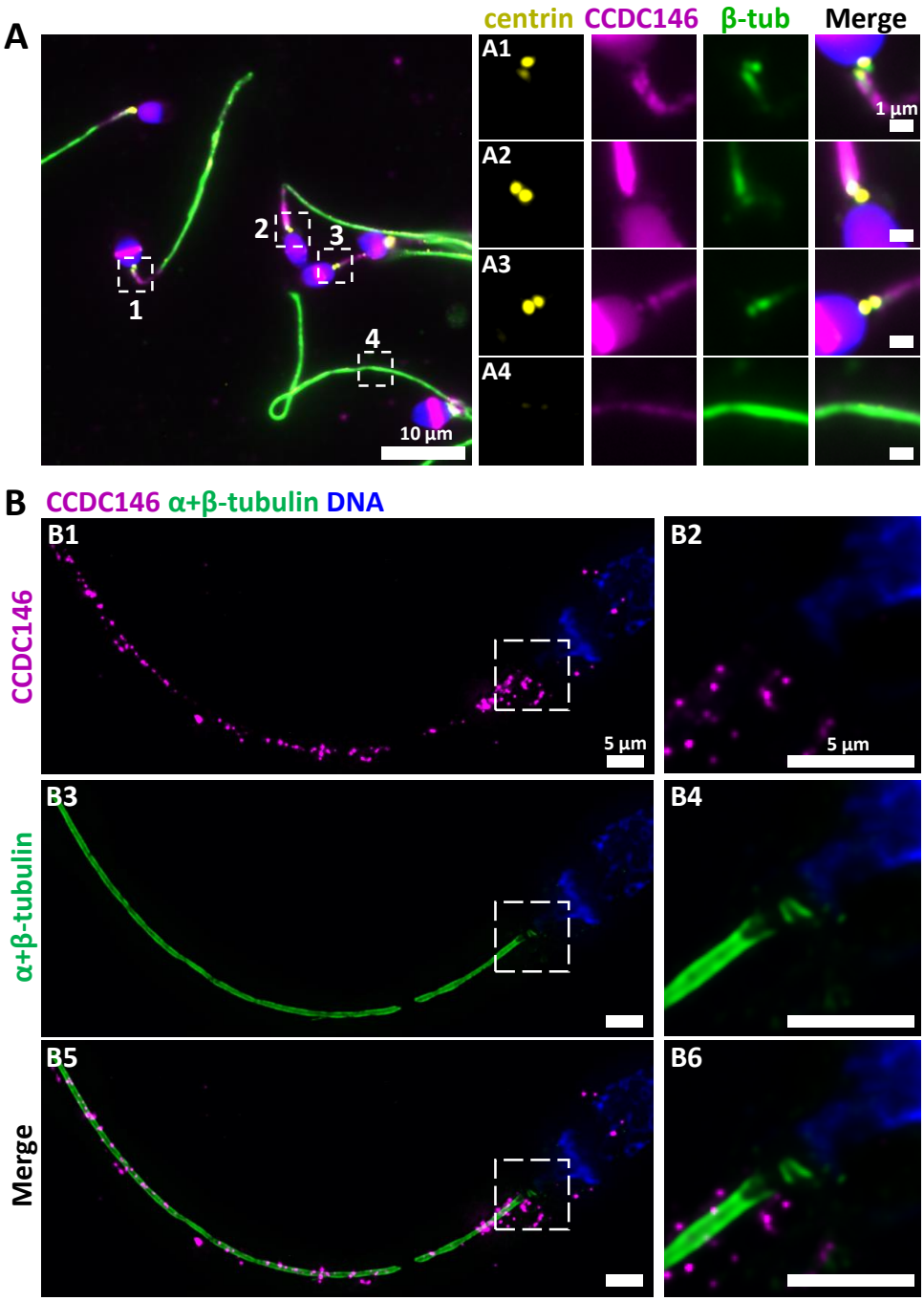
A
centrin
CCDC146
β-tub
Merge
A1
A2
A3
A4
1
2
3
4
10 µm
1 µm
B
CCDC146 α+β-tubulin DNA
CCDC146
α+β-tubulin
Merge
B1
B2
B3
B4
B5
B6
5 µm
5 µm

Figure 8

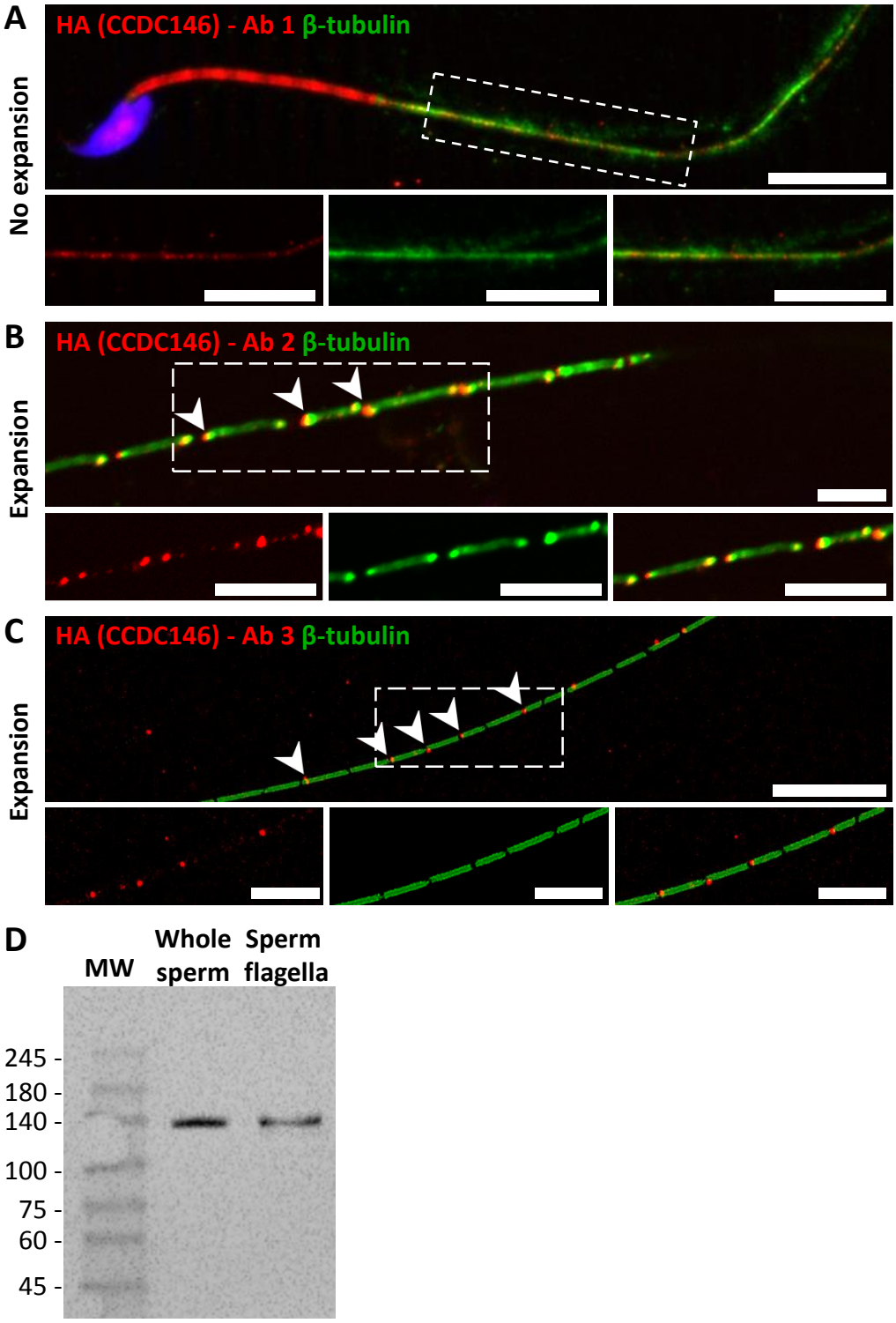
A
No expansion
HA (CCDC146) - Ab 1 β-tubulin
B
Expansion
HA (CCDC146) - Ab 2 β-tubulin
C
Expansion
HA (CCDC146) - Ab 3 β-tubulin
D
MW
Whole sperm
Sperm flagella
245
180
140
100
75
60
45

Figure 9

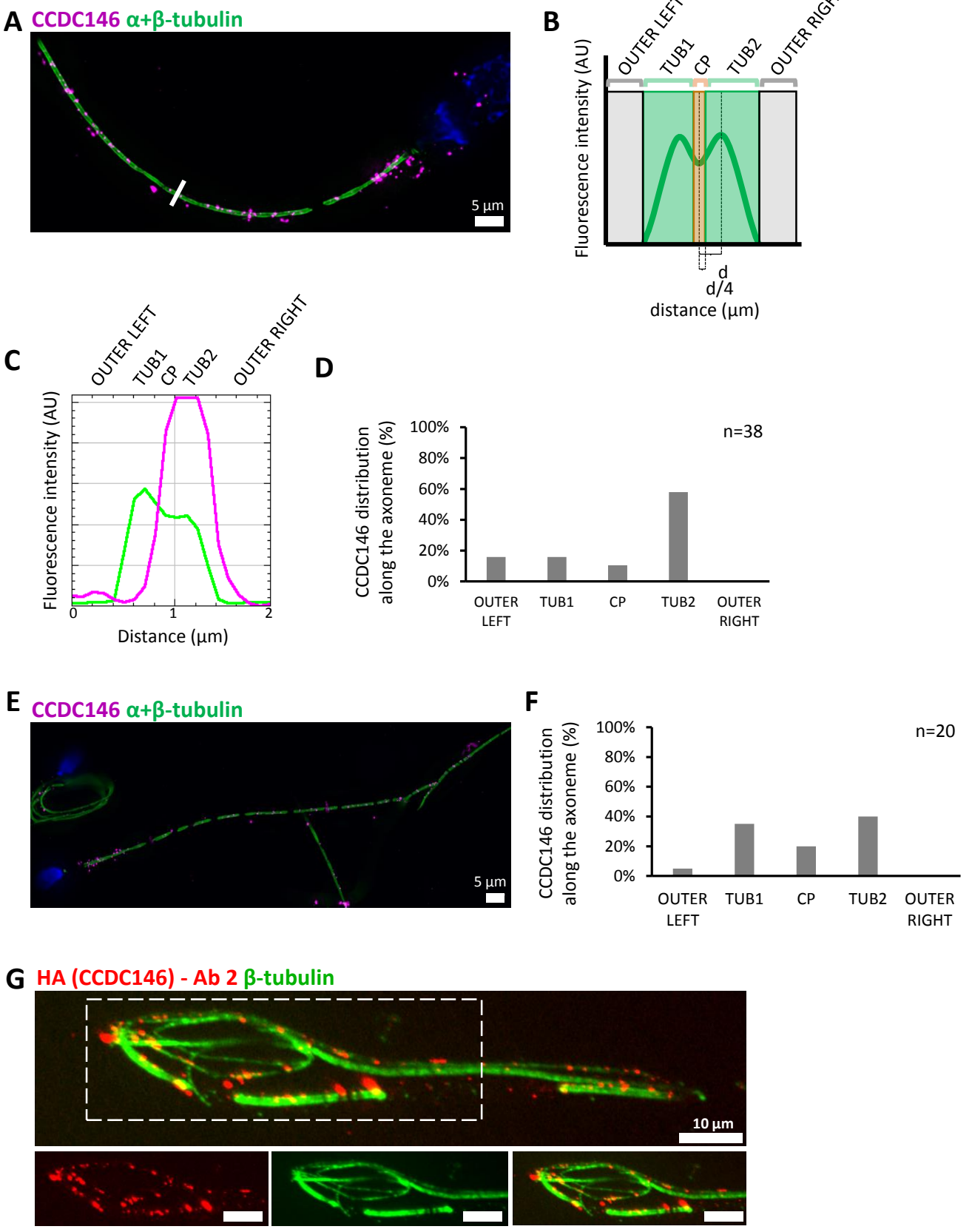
A
CCDC146 α+β-tubulin
5 µm
B
OUTER LEFT
TUB1
CP
TUB2
OUTER RIGHT
Fluorescence intensity (AU)
d
d/4
distance (µm)
C
OUTER LEFT
TUB1
CP
TUB2
OUTER RIGHT
Fluorescence intensity (AU)
0
1
2
Distance (µm)
D
CCDC146 distribution along the axoneme (%)
100%
80%
60%
40%
20%
0%
n=38
OUTER LEFT
TUB1
CP
TUB2
OUTER RIGHT
E
CCDC146 α+β-tubulin
5 µm
F
CCDC146 distribution along the axoneme (%)
100%
80%
60%
40%
20%
0%
n=20
OUTER LEFT
TUB1
CP
TUB2
OUTER RIGHT
G
HA (CCDC146) - Ab 2 β-tubulin
10 µm

Figure 10

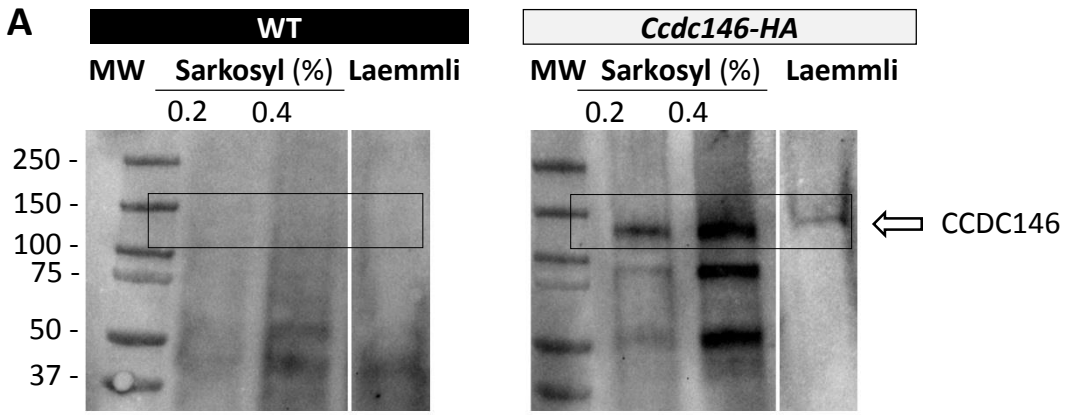
A
WT
Ccdc146-HA
MW
Sarkosyl (%)
Laemmli
0.2
0.4
250 -
150 -
100 -
75 -
50 -
37 -
CCDC146

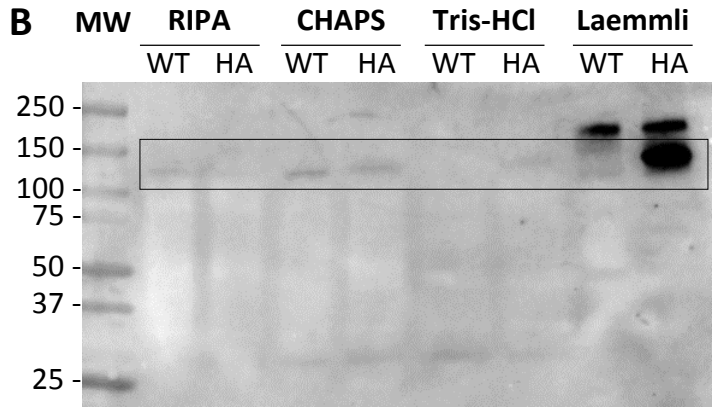
B
MW
RIPA
CHAPS
Tris-HCl
Laemmli
WT
HA
250 -
150 -
100 -
75 -
50 -
37 -
25 -

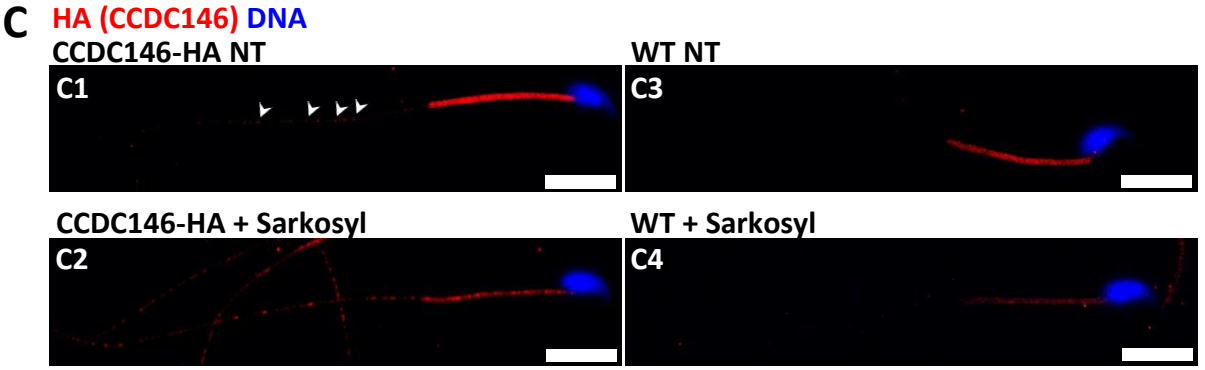
C
HA (CCDC146) DNA
CCDC146-HA NT
WT NT
C1
C3
CCDC146-HA + Sarkosyl
WT + Sarkosyl
C2
C4

Figure 11

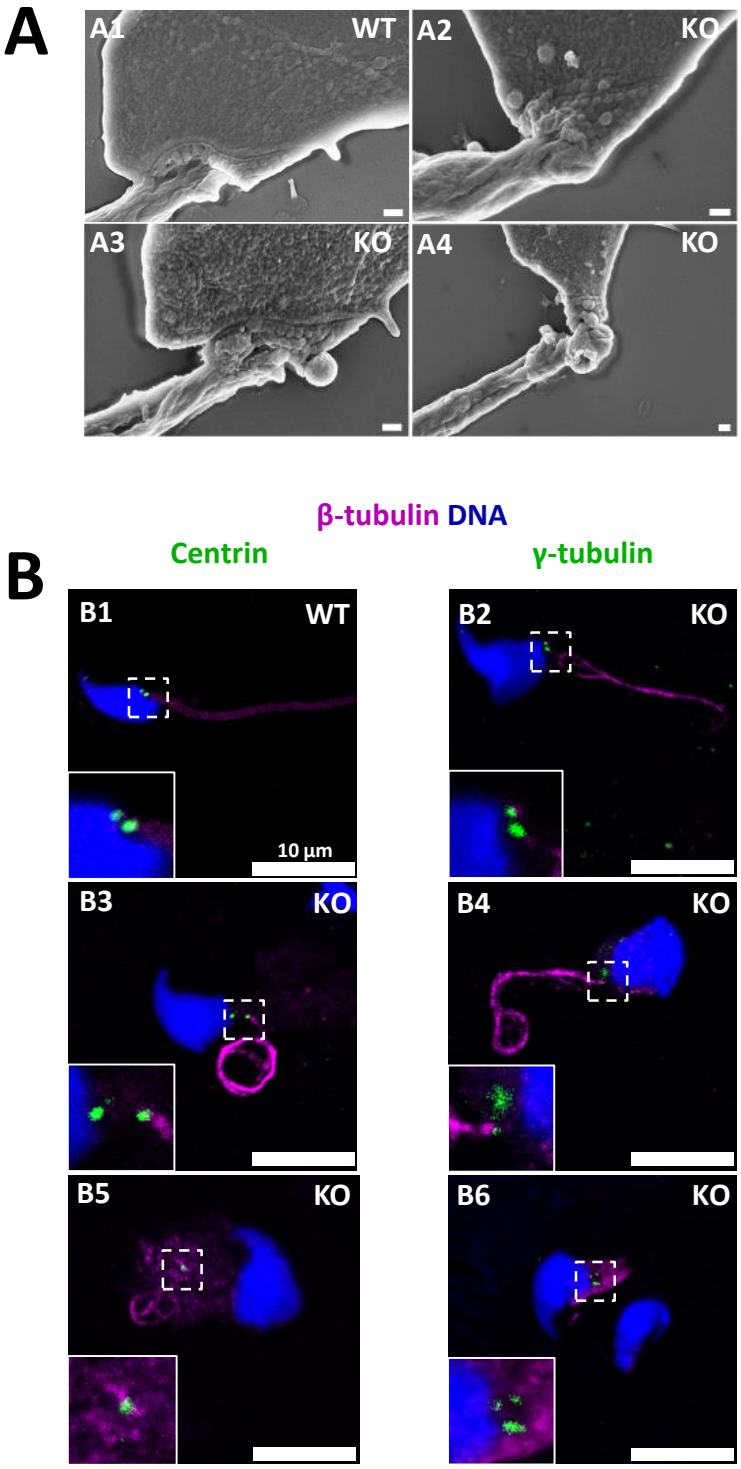
A
A1
WT
A2
KO
A3
KO
A4
KO
β-tubulin DNA
B
Centrin
γ-tubulin
B1
WT
B2
KO
10 µm
B3
KO
B4
KO
B5
KO
B6
KO

Figure 12 - JM

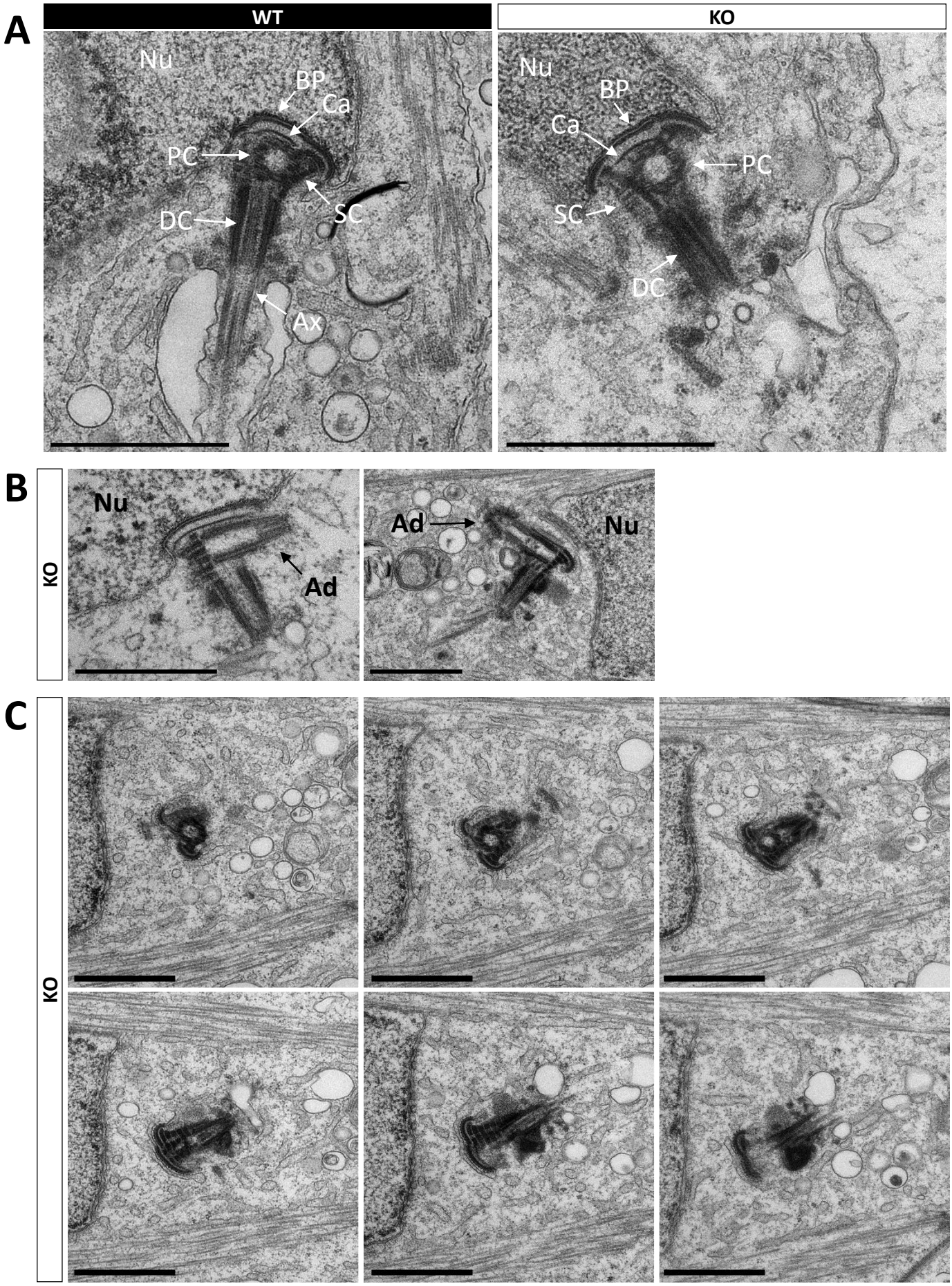

Figure 13

A

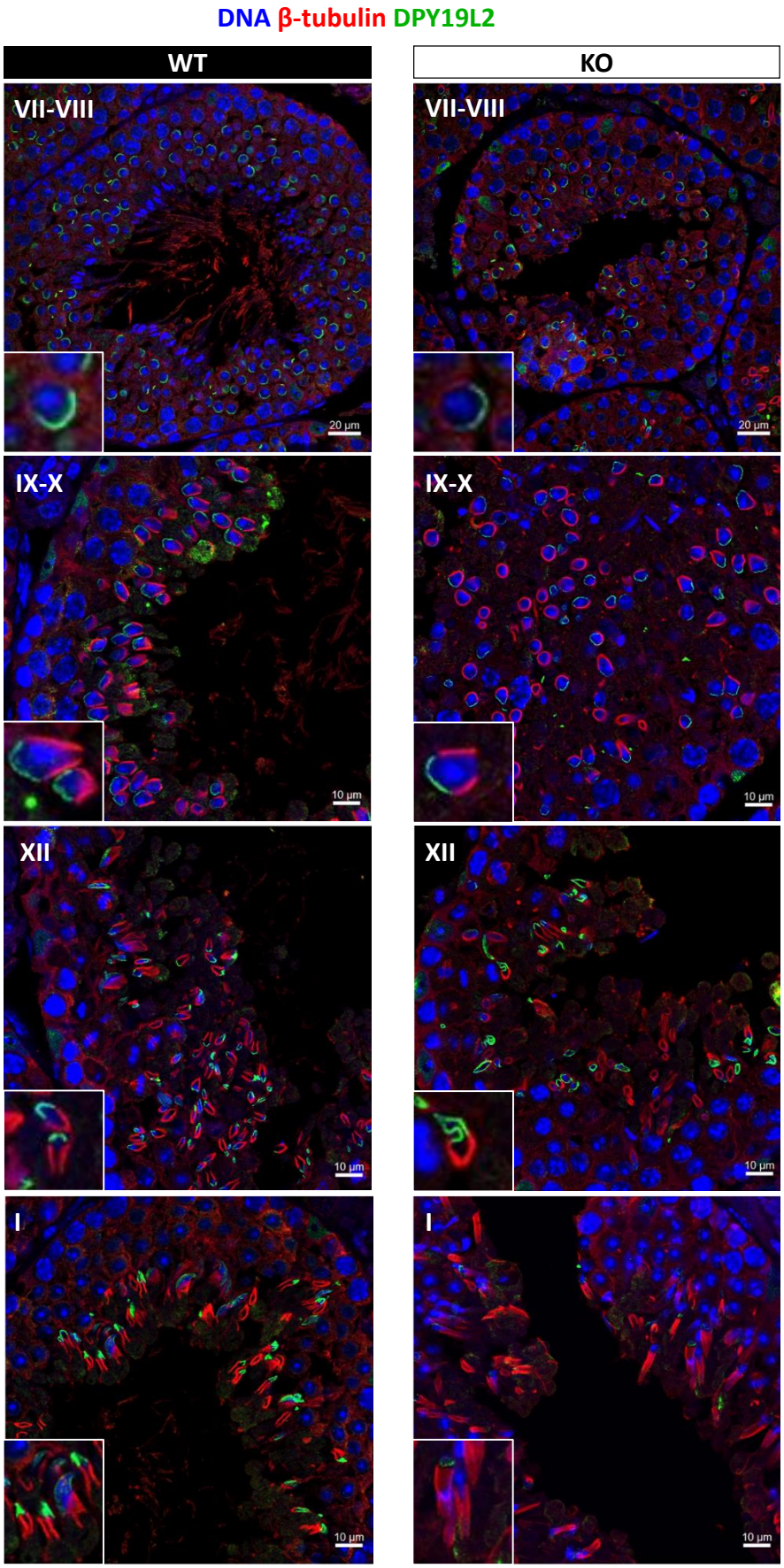
DNA β-tubulin DPY19L2
WT
KO
VII-VIII
VII-VIII
20 µm
20 µm
IX-X
IX-X
10 µm
10 µm
XII
XII
10 µm
10 µm
I
I
10 µm
10 µm

Figure 14

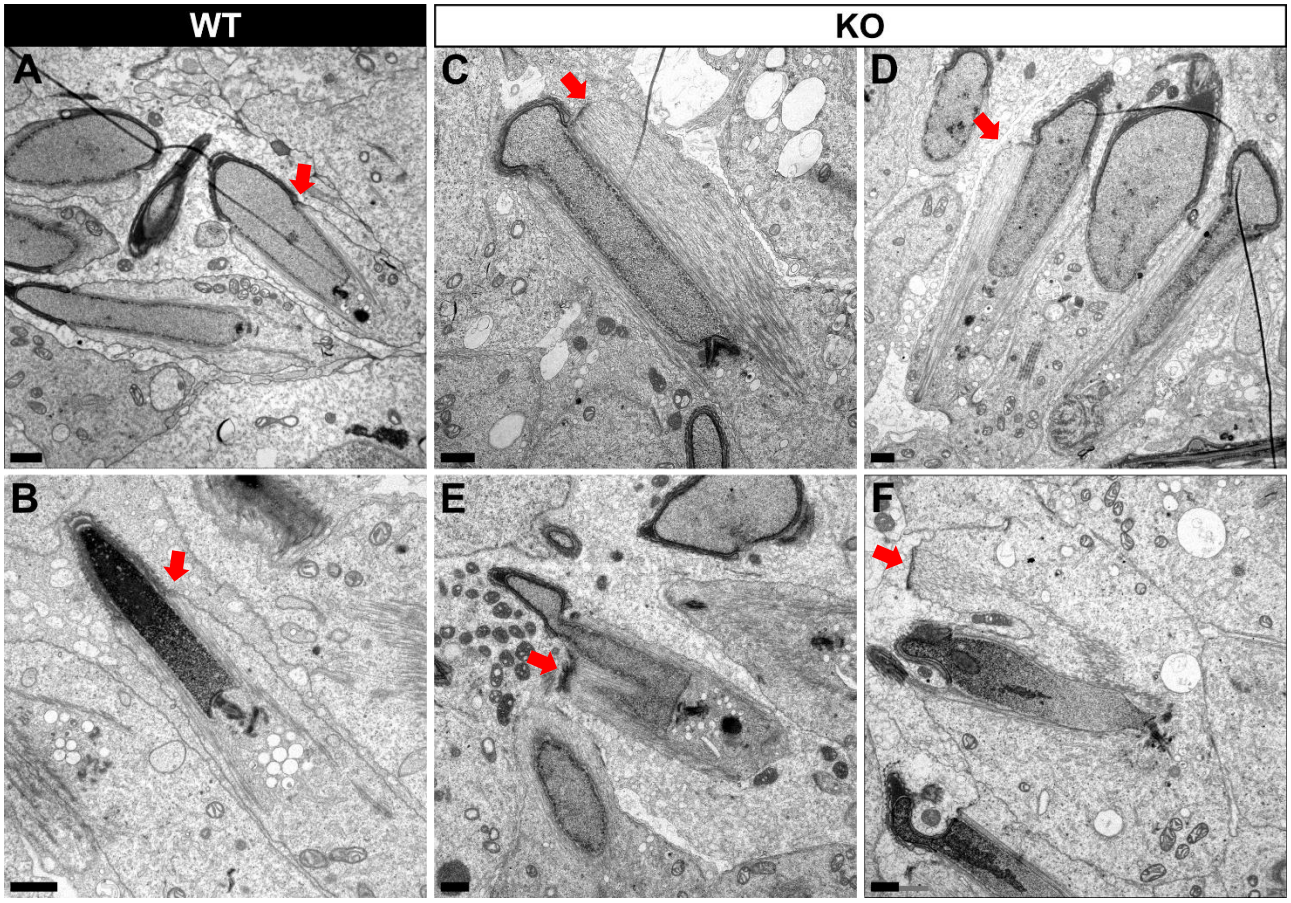

Figure 15

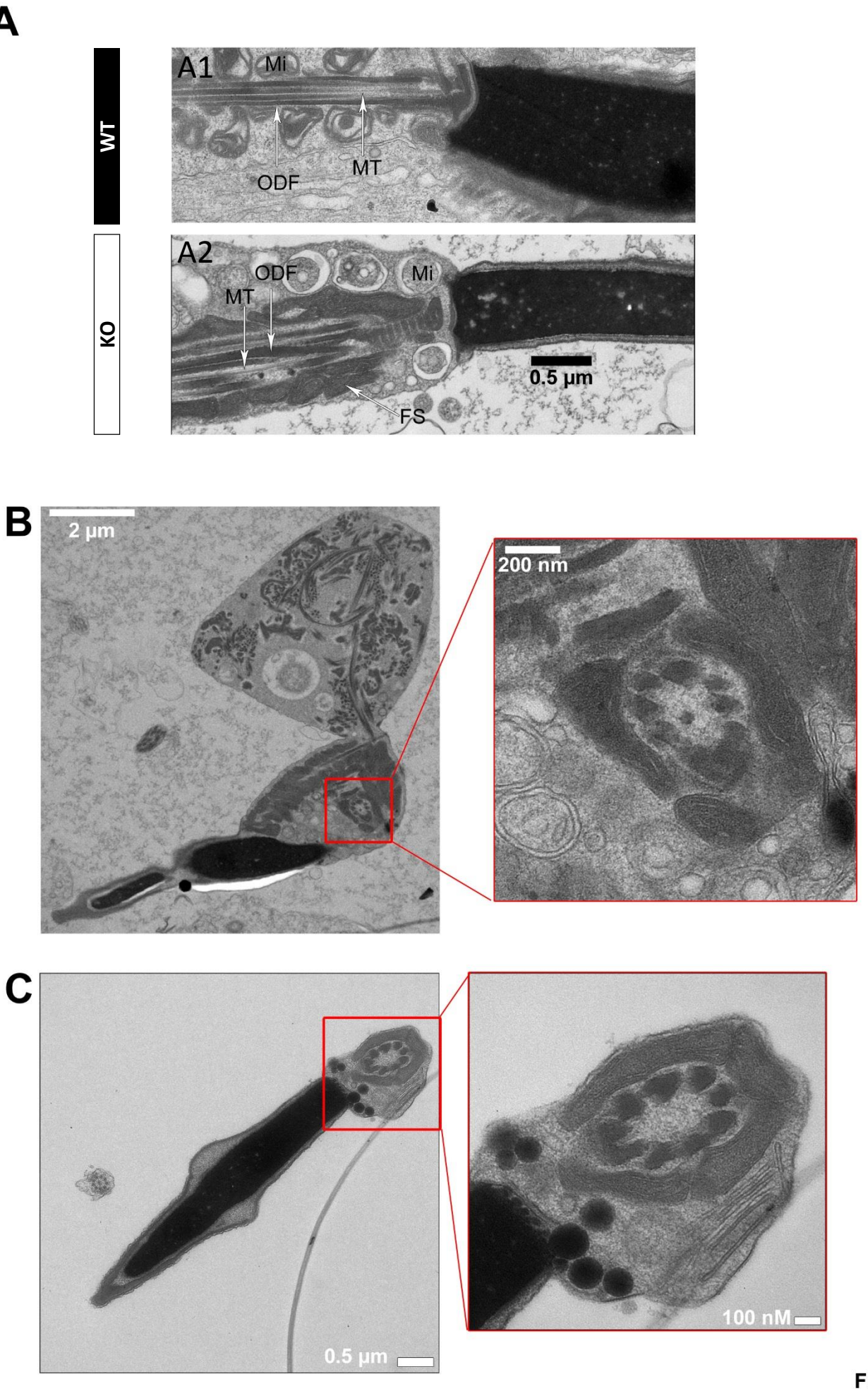

Figure 15

Appendix – Figure 1

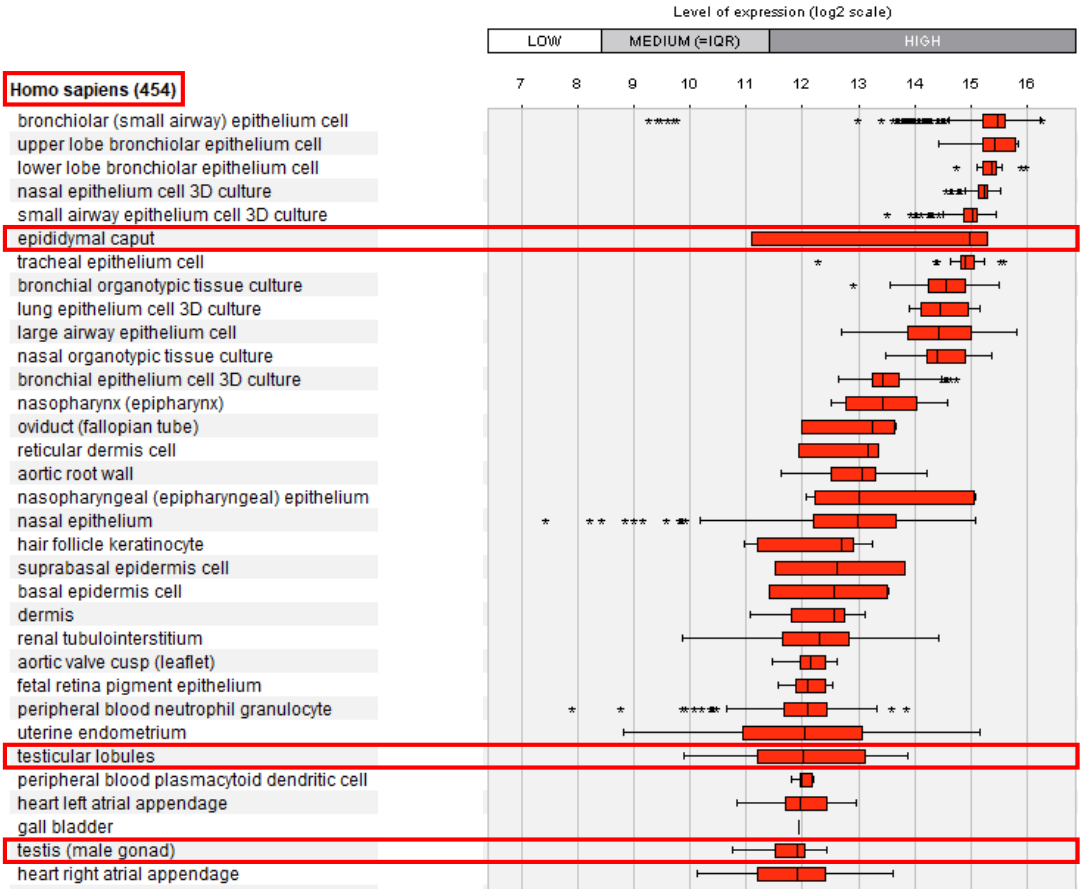

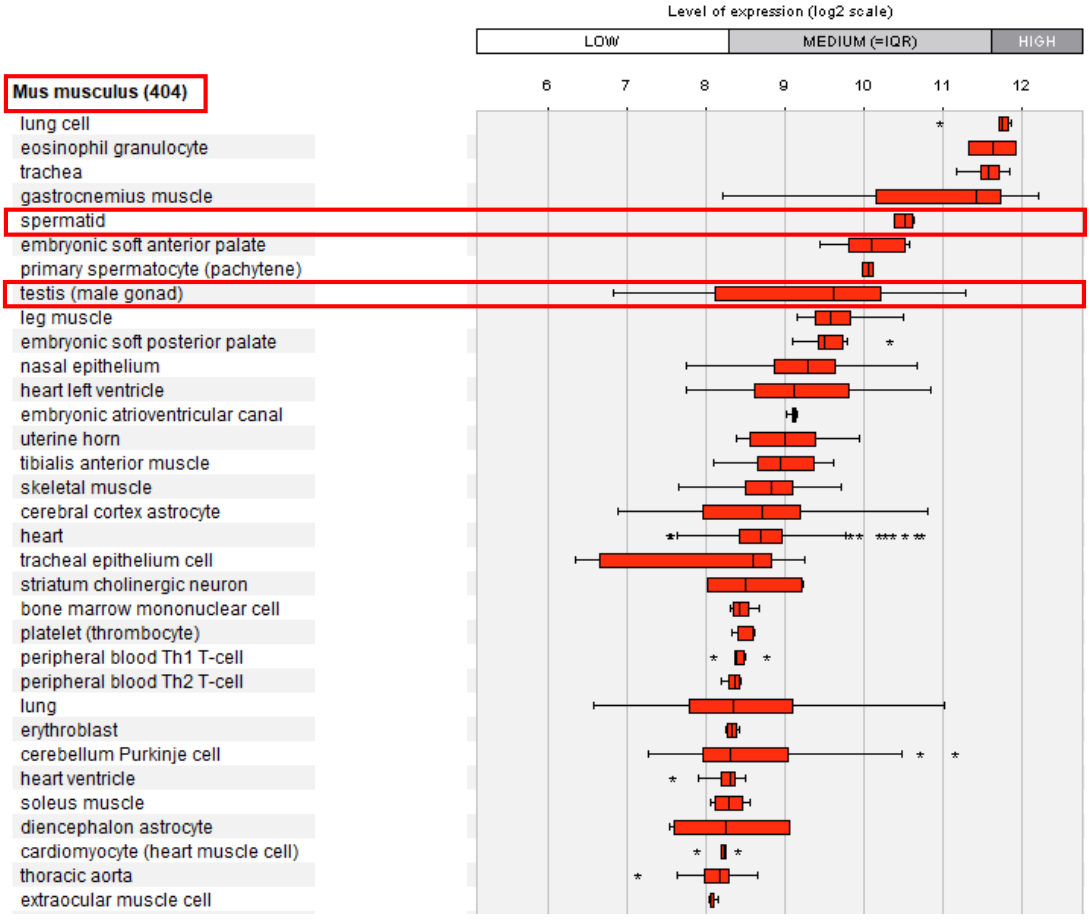

Appendix – Figure 2

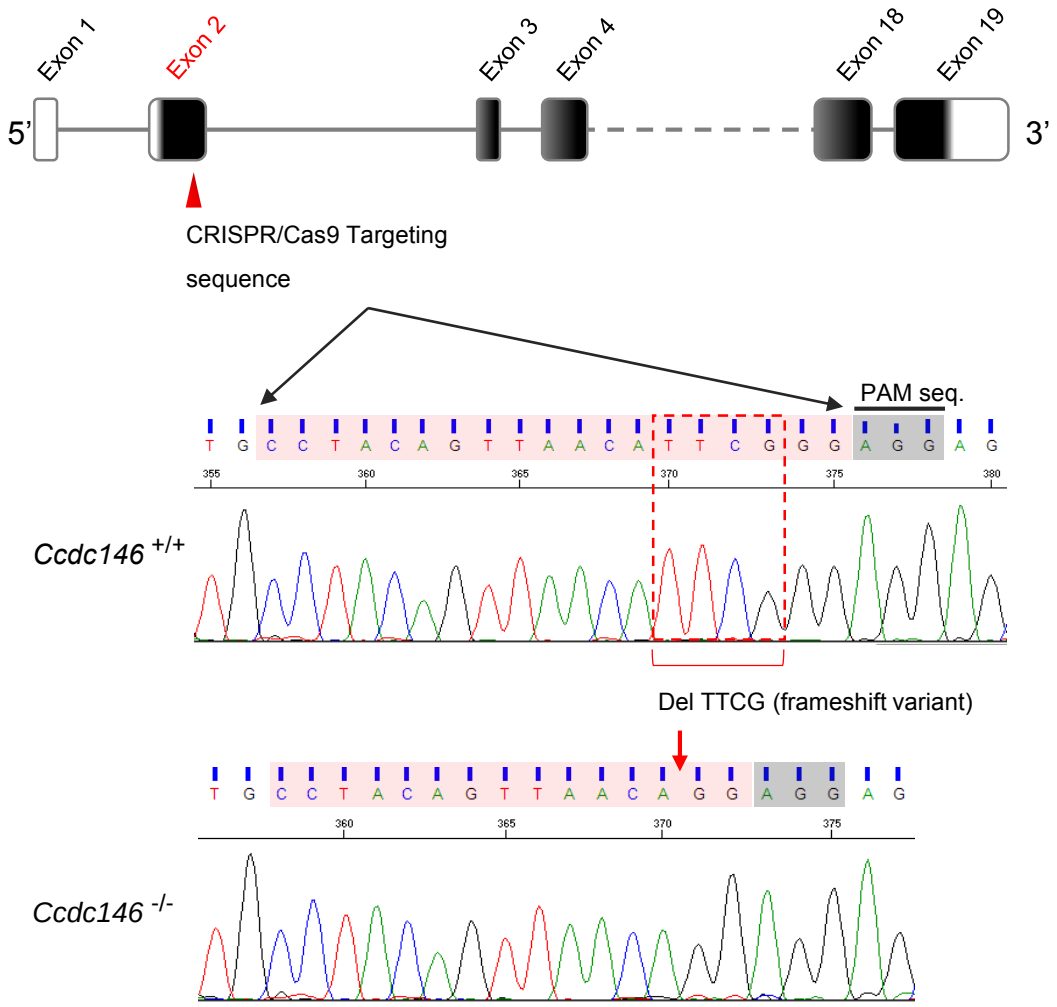

Appendix – Figure 3

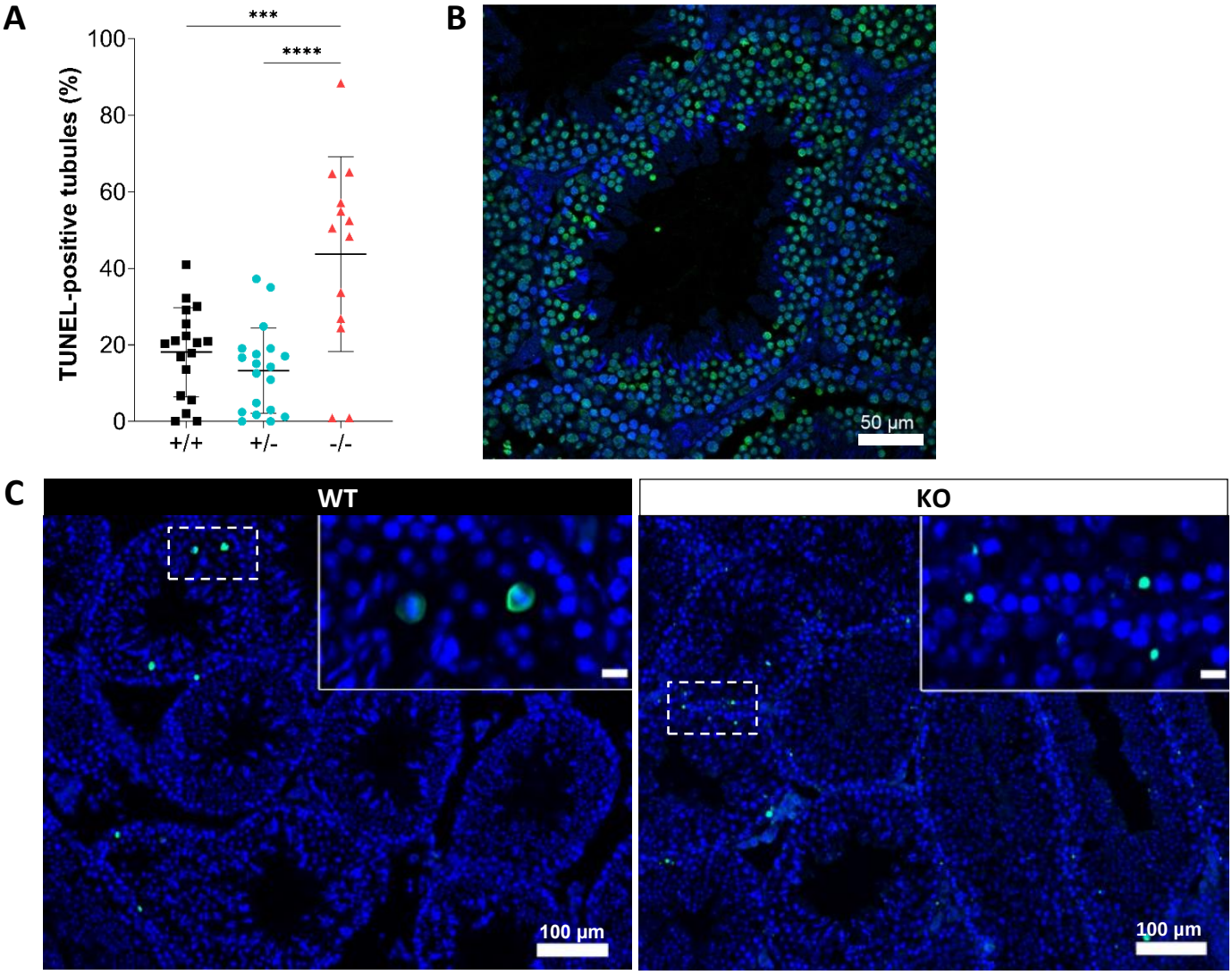

Appendix – Figure 4

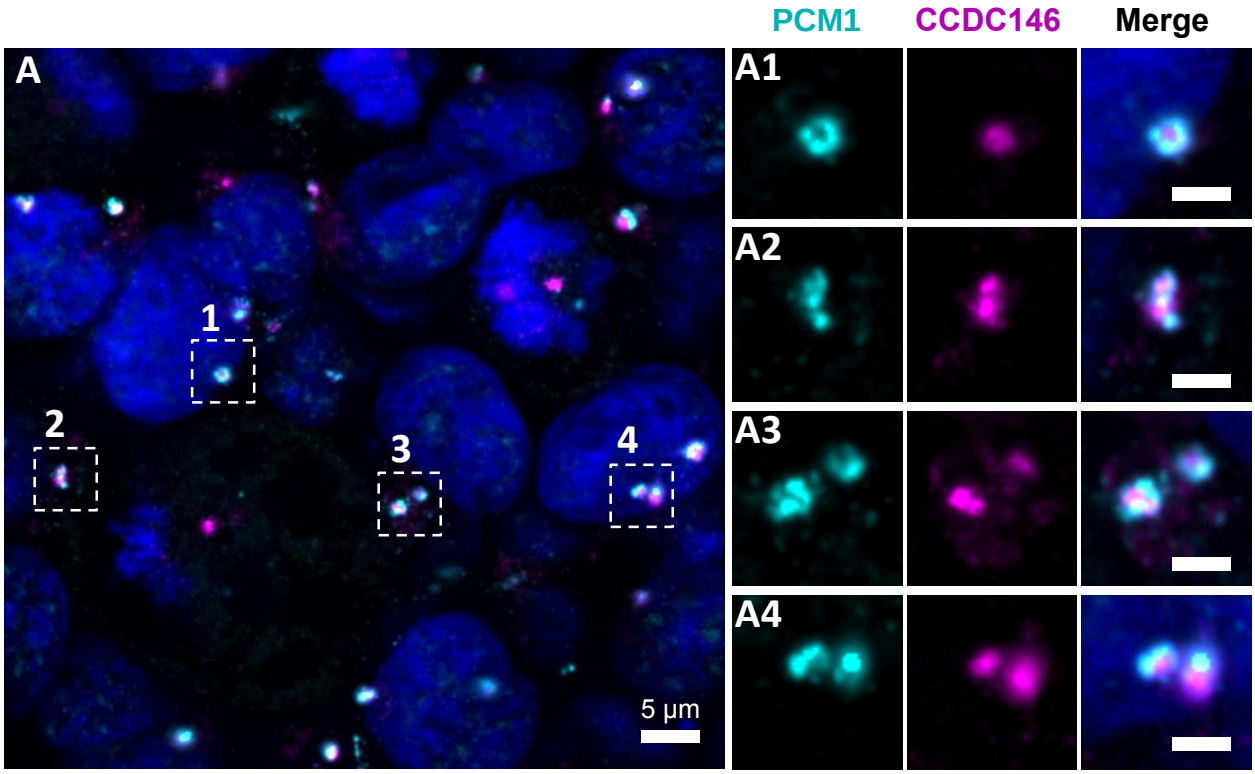

Appendix – Figure 5

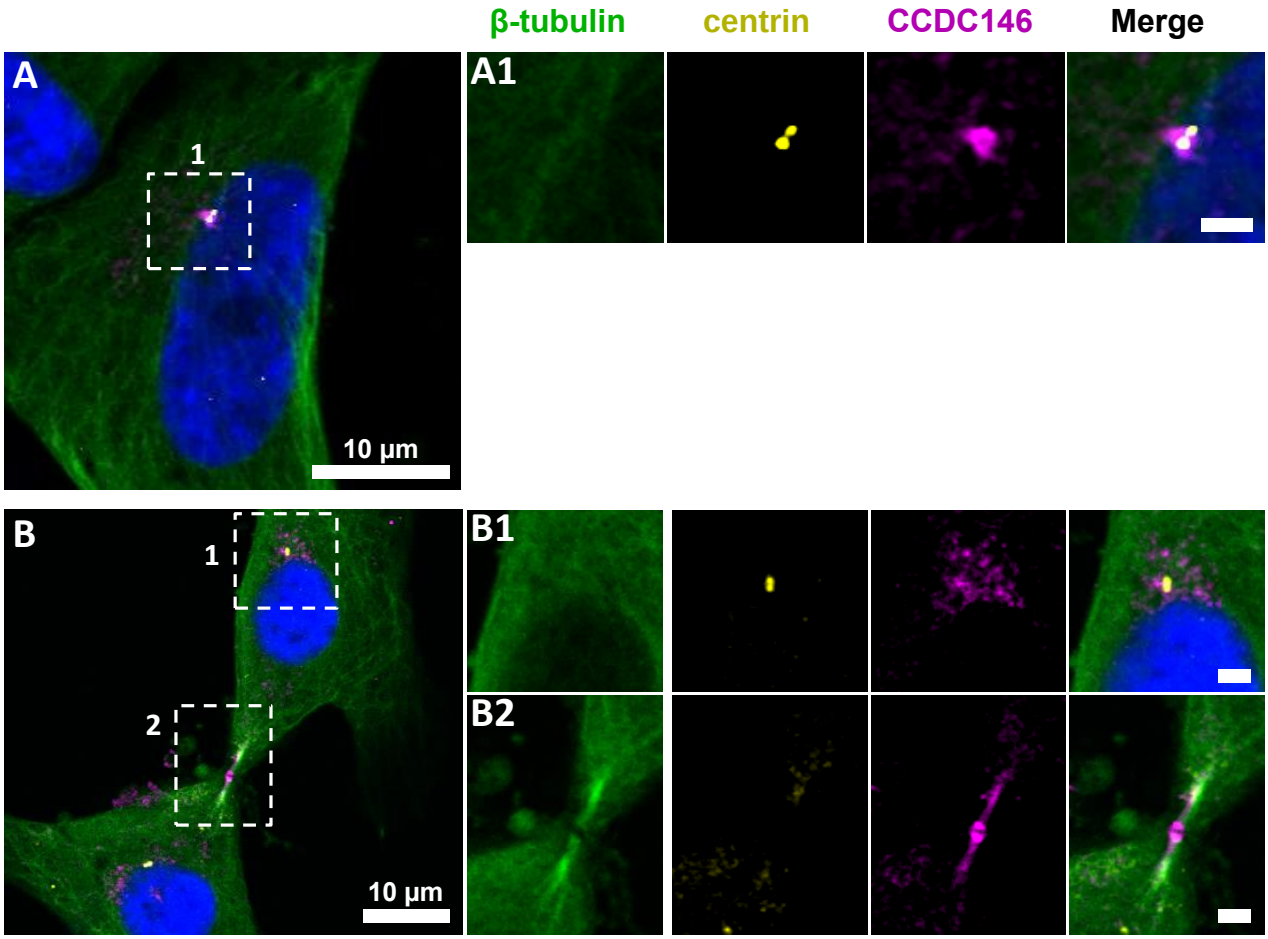

Appendix – Figure 6

Ccdc146 : Knock-in Edits

Transcript: ENSMUST00000115245.7 (GRCm38.p6)

Guide RNA design

TACTTTAGAACTGTGAAAAATGG (in red, the start codon in exon 2/19)

HA Tag sequence

Coding sequence (5'-3') : TAC CCA TAC GAT GTT CCA GAT TAC GCT

Amino-acid sequence (N-C ter) : Y P Y D V P D Y A

Strand	Sequence	PAM	On-target score	Off-target score
+	TACTTTAGAACTGTGAAAAA	TGG	27.9	29.0

1) Tag insertion :

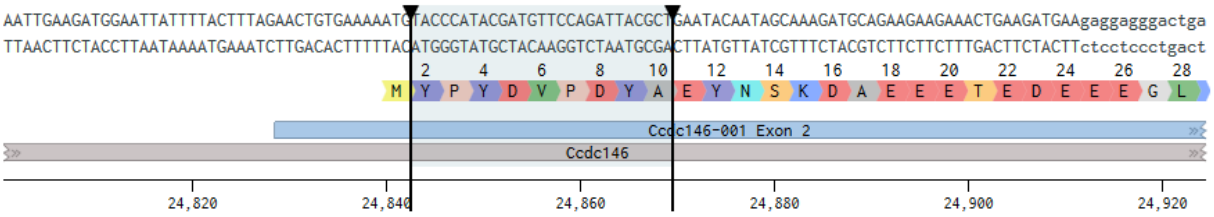

Appendix – Figure 7

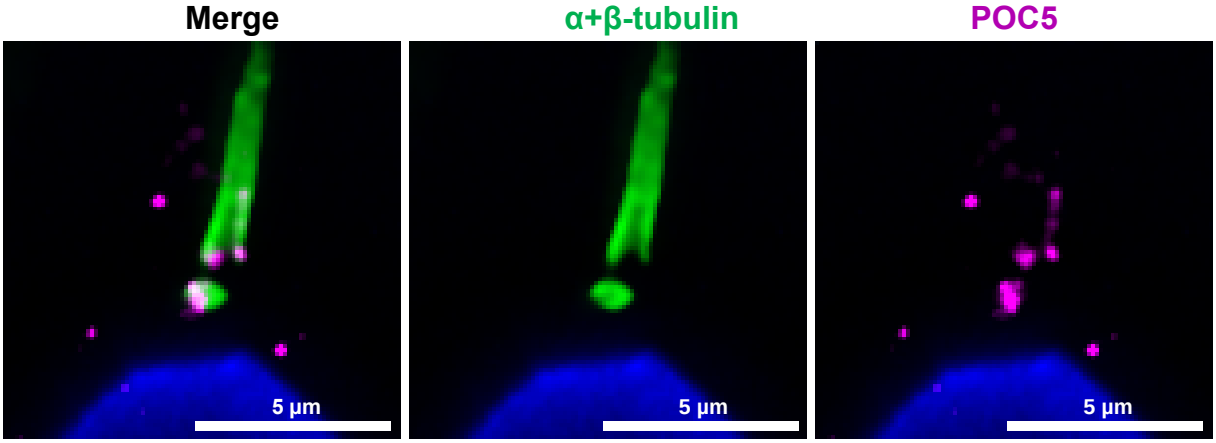

Appendix – Figure 8

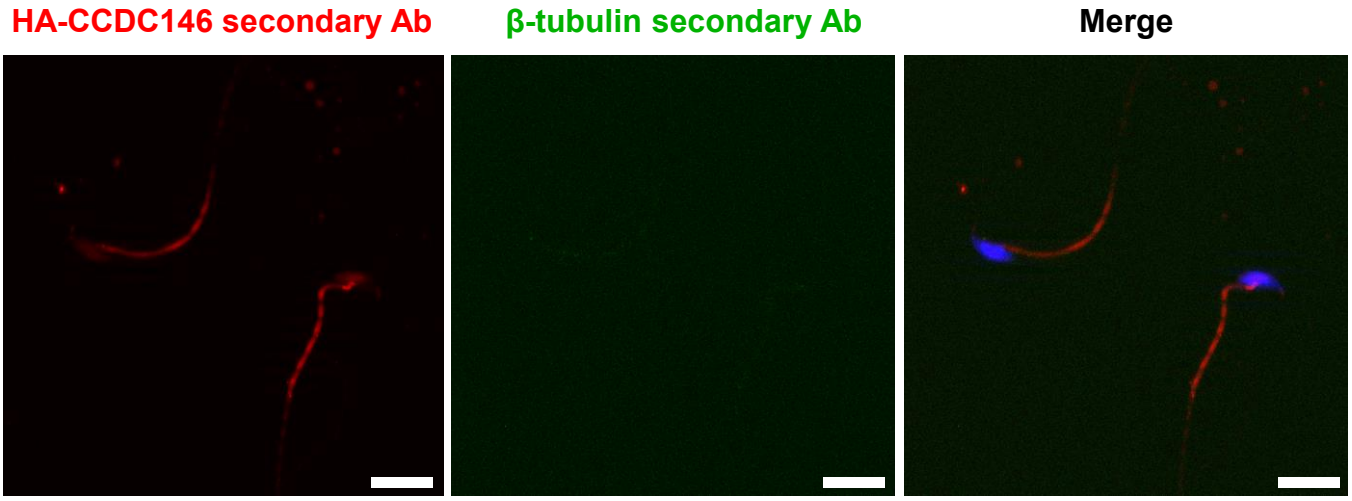

Appendix – Figure 9

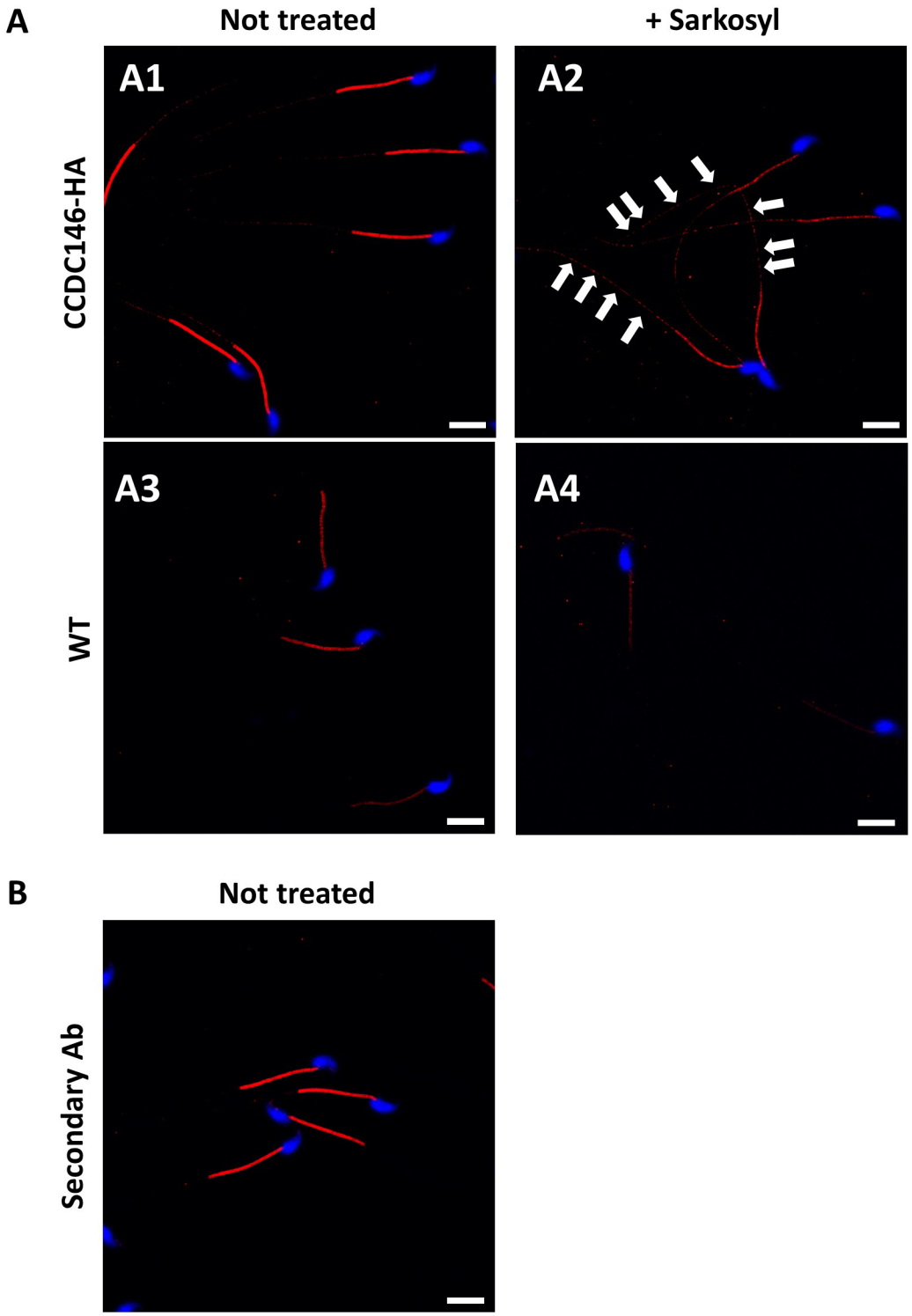

Appendix – Figure 10

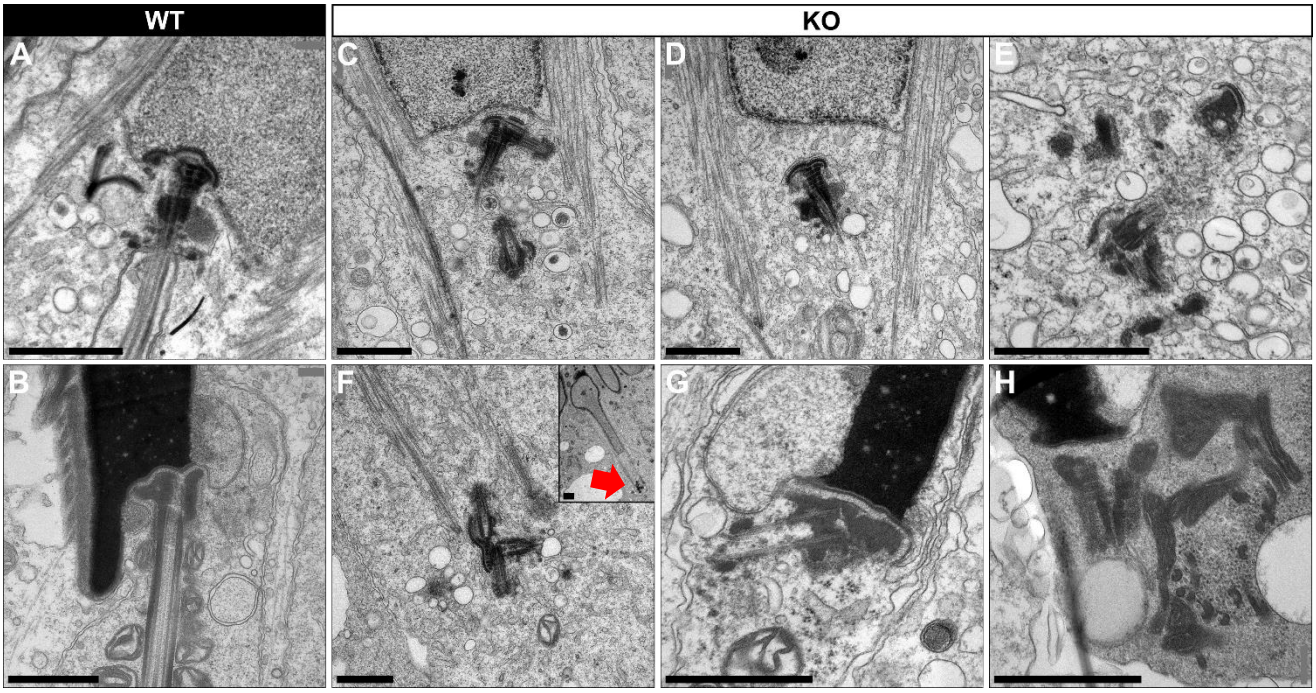

Appendix – Figure 11

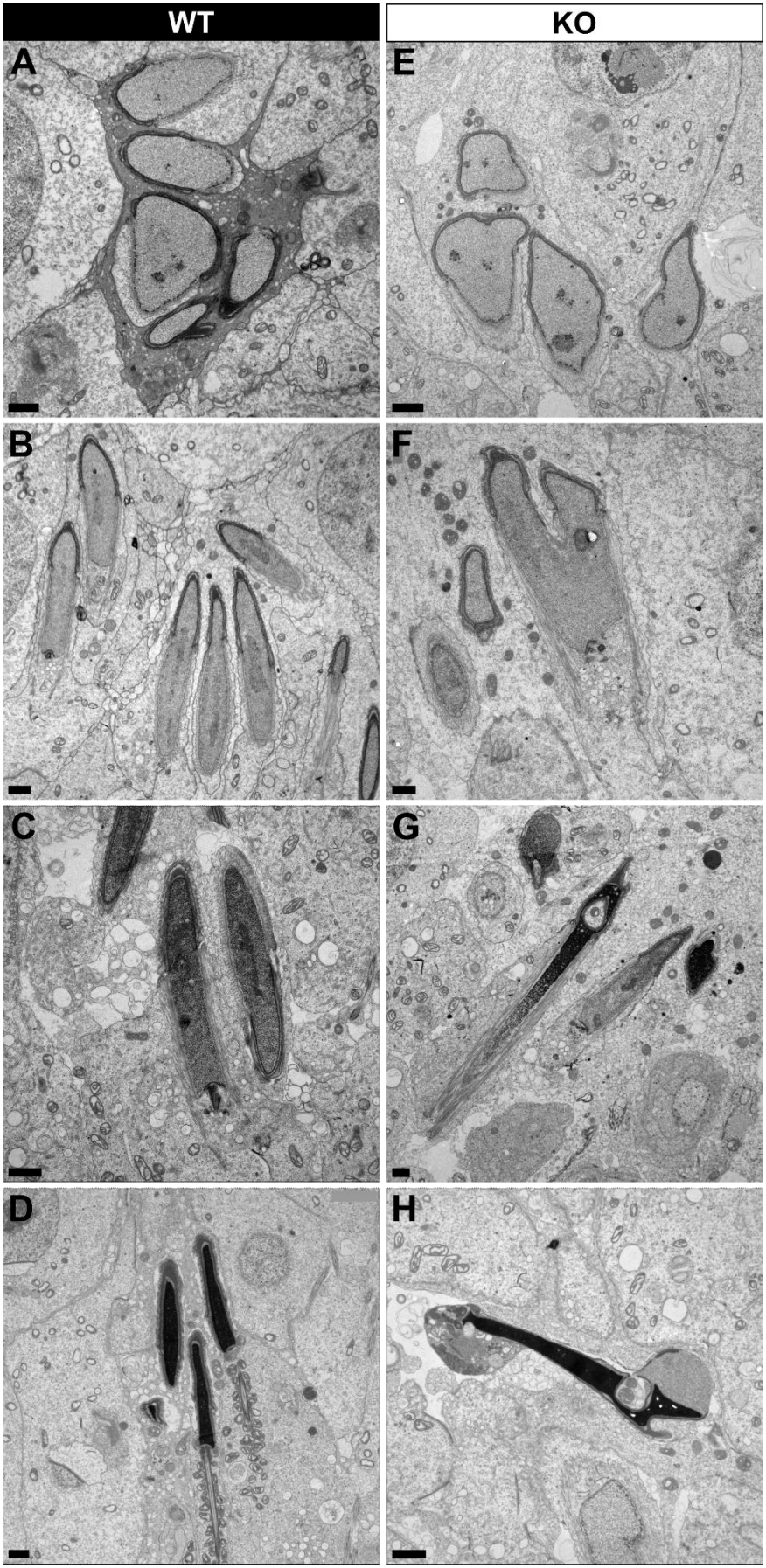

Table Supplementary 1

List of primers used for Sanger verification of the identified variants by WES.

Primer name	Primer sequence (5'-3')	Tm (°C)	Product length (bp)
CCDC146-Int8F	ATTGCTGGGTCAAACGGTAG	57.3	422
CCDC146-Int9R	GGCAGCAAAAACAACTTCCT	55.3	
CCDC146-Ex15F	CAGCTGATAGAGCGGGAAGA	59.3	457
CCDC146-Int15R	TCCAAGAAAAGCAGAAAATGC	54.0	

List of primers used for knock-out mice genotyping.

Primer name	Primer sequence (5'-3')	Tm (°C)	Product length (bp)
Ccdc146-Ex2F3	GGGAGGAACAGGAGAAGGAG	61.4	151
Ccdc146-Ex2R3	TCATGCAGACAGAGGAAAGC	57.3	

List of primers used for knock-in mice (HA-Tag) genotyping.

Primer name	Primer sequence (5'-3')	Tm (°C)	Product length (bp)
shCCD_ki-F1	ACTTGGTGGGTGTTGTCCTA	58.49	149
shCCD_ki-R1	TCCCTCCTCTTCATCTTCAGT	57.52	
lgCCD_ki-F1	AGAAATCAGGGAGGGGTTGC	59.67	504
lgCCD_ki-R1	AATTGATGAGCCGCTCCTCC	60.18	